POLITECNICO DI MILANO

Scuola di Ingegneria dei Processi Industriali

Corso di Laurea Specialistica in
Ingegneria Nucleare

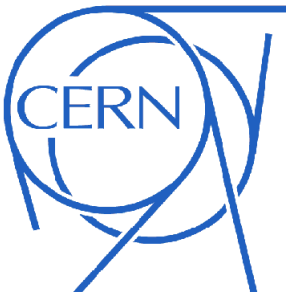

COPPER FOR PARTICLE ACCELERATORS: ELECTRON STIMULATED DESORPTION AND STUDY OF HYDROGEN CONTENT MEASUREMENT BY LASER ABLATION

Relatore: Prof. Marco BEGHI
Correlatore: Dr. Sergio CALATRONI

Master Degree Thesis of:
Irene MARTINI matr. 751009

Academic Year 2010-2011

Abstract

This Master thesis work has been carried out in the Vacuum, Surface and Coating group of CERN in the framework of the CLIC (Compact Linear Collider) project. In particle accelerators strict requirements concerning the static and dynamic pressure have to be fulfilled, in order to avoid interaction of the beam with residual gas molecules.
CLIC accelerating structures are designed as modular copper cavities which have to sustain a high electric field. The high accelerating gradient conceived for CLIC has raised the problem of electron field emission and resulting stimulated desorption from the surface of the cavities. These phenomena lead to bursts of pressure which are local and of short time scale, therefore not easily detectable.

The first part of this work aims to test unbaked copper by electron stimulated desorption for electron energies up to 10 keV. The results have been compared to previously recorded data from a differently treated sample. Moreover, improvements to the measurement process and to the experimental system have been implemented in order to increase the system performance.
The second part deals with the investigation of hydrogen content measurement by laser ablation.
During the bonding procedure of the CLIC cavities performed at high temperature in hydrogen atmosphere, the hydrogen can easily diffuse in the copper bulk. The investigated method consists of ablating a known amount of material from copper samples, previously treated in the same conditions of the cavities, while recording the hydrogen partial pressure by a mass spectrometer in order to measure the hydrogen content in the material.

In Chapter 1 an overview on the CLIC project, related studies in the field of dynamic vacuum effects and the copper sample campaign is given.
Chapter 2 deals with the physical background of both electrons stimulated desorption (ESD) and laser-target interaction during ablation. Moreover an introduction to solubility, particularly for hydrogen-copper systems is given in the third section.
In Chapter 3 the ESD experimental setup, the measurement procedure and the data are presented.
In Chapter 4, the laser ablation setup is described in detail as well as the efforts done to investigate, estimate and reduce the parasitic source of hydrogen which limits the measurement.

Abstract

Il presente lavoro di laurea è stato sviluppato in collaborazione con il gruppo Vacuum Surface and Coating del CERN nell'ambito del progetto CLIC (Compact Linear Collider).
Negli acceleratori di particelle devono essere soddisfatti severi requisiti dal punto di vista della pressione statica e dinamica per evitare interazioni tra il fascio e le molecole di gas residuo.
Le strutture acceleranti di CLIC sono progettate come cavità modulari di rame e devono essere in grado di sostenere elevati campi elettrici. L'elevato gradiente di accelerazione previsto per le strutture acceleranti di CLIC ha sollevato il problema dell'emissione di elettroni per effetto di campo e del desorbimento stimolato dalle superficie delle cavità associato. Questi fenomeni inducono picchi di pressione localizzati e temporalmente brevi al punto da non essere facilmente rilevabili.

Nell'ambito della prima parte del presente lavoro è stato caratterizzato il desorbimento indotto da elettroni sul rame, nello specifico su rame non precedentemente sottoposto a processi di bake-out e con elettroni ad energie fino a 10 keV. I risultati ottenuti sono stati confrontati con quelli acquisiti per un altro campione, anch'esso di rame ma sottoposto ad un diverso trattamento chimico e termico. Inoltre sono state apportate alcune migliorie al metodo di misurazione e all'apparto sperimentale per rendere le misure più affidabili.
La seconda parte del presente lavoro, invece, è stata dedicata all'investigazione della fattibilità e l'applicabilità del metodo di ablazione laser per misure di contenuto di idrogeno.
Durante i cicli di assemblaggio delle cavità di CLIC eseguiti ad alta temperatura in atmosfera di idrogeno, l'idrogeno può facilmente diffondere all'interno del rame.

La tecnica investigata prevedede di ablare una quantita' nota di materiale da provini di rame, precedentemente sottoposti algli stessi trattamenti delle cavità, e misurare l'aumento della pressione parziale di idrogeno con uno spettrometro di massa per risalire alla quantità di idrogeno presente nel materiale.

Nel primo capitolo è fornita una panoramica sul progetto CLIC, gli studi degli effetti dinamici di vuoto e le caratteristiche dei campioni della campagna di test associata.
Il secondo capitolo tratta delle basi fisiche del desorbimenno indotto da elettroni (ESD) e dei fenomeni di interazione di un fascio laser intenso con un bersaglio di materiale solido. Inoltre, è introdotto il concetto di solubilità nel caso specifico del sistema idrogeno-rame.
La descrizione dell'apparato sperimentale utilizzato per le misure di desorbimento indotto da elettroni, così come i risultati ottenuti, sono discussi nel terzo capitolo.
Nel quarto capitolo è descritto nel dettaglio l'apparato sperimentale utilizzato per l'ablazione laser così come sono discussi i tentativi volti ad indagare, stimare e ridurre la fonte parassita di idrogeno che limita le potenzialità di questo metodo di misura.

Contents

List of Figures

List of Tables

Chapter 1

Introduction

The present Master thesis has been carried out in the Vacuum Surface and Coating Group at CERN (European Organitazion for Nuclear Research, Geneva) in the framework of CLIC (Compact Linear Collider) project.
Hereafter the CLIC construction plans and a summary of the studies linked to dynamic vacuum effects in its accelerating structure will be introduced.

1.1 CLIC project at CERN

CLIC is a study for a future electron-positron room temperature linear collider 50 km long[1]. Several important partners are involved in this worldwide collaboration: the International Linear Collider project (ILC); the Standford Linear Accelerator Center (SLAC) in California (USA); the High Energy Accelerator Research Organization (KeK) in Tsukuba (Japan). The design of CLIC is calling for a electron-positron collisions up to a nominal center-of-mass energy of 3 TeV.
The range of energy is the same of LHC (Large Hadron Collider), but using electrons and their antiparticles, instead of protons, would lead to gain complementary knowledges. Linear colliders are characterized by an higher experimental precision. High energy collision requires highly accelerated particles. The CLIC accelerator is conceived in order to reach an accelerating gradient of 100 MV/m in the accelerating structure because a lower gradient would need longer structure and therefore additional length of the machine. Choosing this high gradient raises several problems and challenges from the design of Radio Frequency power supply to the accelerating structure design, from material studies to vacuum related issues.

This accelerator is called "compact" because of the estimated dimensions: 15 km of accelerating structures, 5 km space for beam injection and quadrupoles and 4 km for beam delivery (cleaning, diagnostics) per each beam, leading to 48 km of total span. The accelerating structure is tuned at the operational frequency of 12 GHZ. The usual RF amplifiers, the so-called Klystrons,are not likely to reach the necessary power level at the above mentioned frequency. This can explain the unique feature of CLIC layout: the two-beam acceleration method. The current layout, characterized by main beam and drive beam, is shown in Figure 1.1. The drive beam is conceived to supply the desired frequency and it is characterized by a high electronic current at a low energy. Passing through the Power Extraction and Transfer Structures (PETS) it is decelerated leading to the acceleration of the mean beam (low current and high energy).

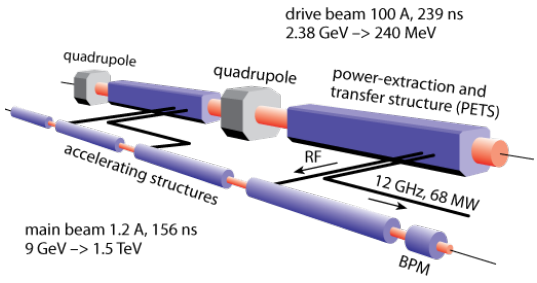

Figure 1.1: CLIC layout(focus on the two-beam acceleration method)

An overview of the whole structure of CLIC layout is shown in Figure 1.2. The main components are: the two injection lines for electrons and positrons, the accelerating structures (two linacs) and the RF power supply structures. The latter is composed by the drive beam accelerators, the PETS and the Kylstrons gallery. The detector will be placed in the interaction point, in the middle of two linear accelerators for monitoring the particles wich come from the interactions. The studies related to the detectors are strictly linked to simulations and to the results that will be collected in the LHC's experiments.
The accelerating structures are designed as travelling wave structures instead of standing accelerating structure. These structures are conceived to work at room temperature because the cryogenic technology cannot be used at this gradient value.

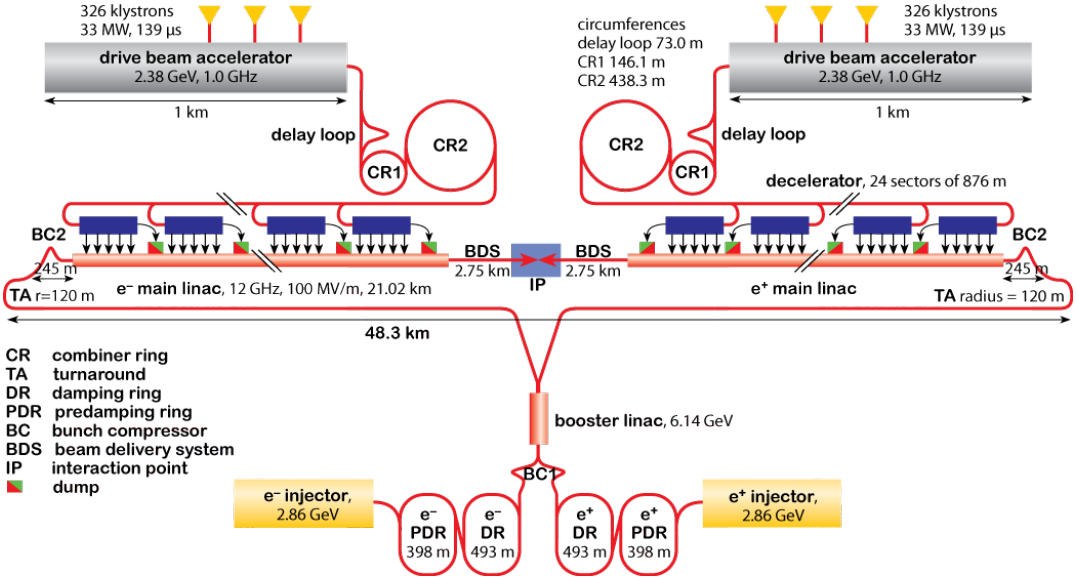

Figure 1.2: CLIC layout

The scheme of Figure 1.2 does not highlight a lot of ancillaries that actually are needed to run an accelerators: the vacuum systems,the focusing system, the cooling system, etc..

In Figure 1.3 a preliminary layout of the pumping group near the accelerating structure is shown. The background pressure planned by the guideline is in the range of 10^{-9} $mbar$ in order to prevent beam interaction with the residual particles. However the accelerating structures are not-baked structures, therefore the baseline pressure is water driven. Moreover the static pressure is limited by the low conductance of the beam pipe (see Figure 1.4).

In Figure 1.3 the quadrupoles for the main beam and drive beam are shown. The specifications of these components are related to the need of a magnetic field shaped in order to focused the beams at a nanometer size.

The alignment is an other important issue for CLIC: about 72000 components have to be aligned with an accuracy ranges from 3 μm to 300 μm depending on the component. To correct the misalignment due to ground motion, noise of the accelerator itself and temperature induced dilations the insertion of active alignment components has been planned.

A scheme of a cooling system module is shown in Figure 1.5: the supply pipe

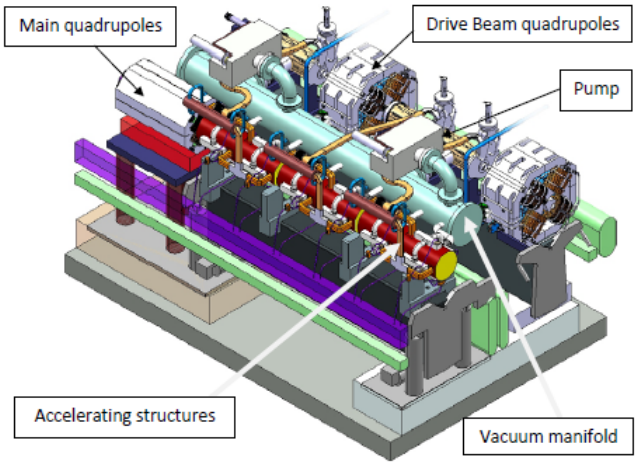

Figure 1.3: CLIC pumping system layout

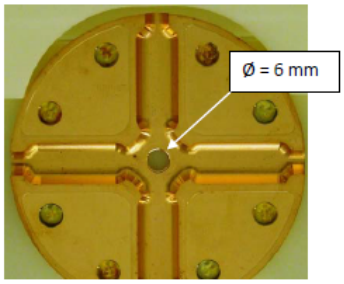

Figure 1.4: Focus on CLIC beam pipe dimension

brings cooling water at 25° C to the accelerator and the return pipe collects water at 45° C. The temperature increase causes several problems, for instance the change in volume of the accelerating structure which in turn leads to a different tuning frequency. The need of temperature control is strictly related to alignment issue and material studies. The main beam-drive beam concept has already been tested as well as several accelerating structures. The CLIC test Facility 3 is a CERN test area where feasibility of the collider is studied.
Finally it has to be mentioned that these and other issues about CLIC are still ongoing activities (more details can be found in [1]).

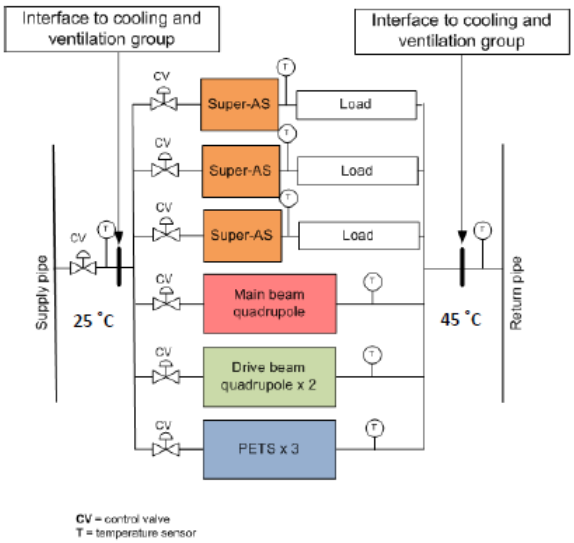

Figure 1.5: CLIC cooling system module type 1

1.2 Dynamic vacuum studies for CLIC accelerating structures

As all accelerators, CLIC has several constraints related to vacuum requirements. It is important indeed reduce the interaction between beam and the residual molecules to prevent beam instability.

The static background pressure in CLIC, as already mentioned, is influenced by both the geometry and the material of accelerating structures. The pumping speed, indeed, is limited by the dimension of the beam pipe section and the choice of not-baked structures leads to have a high content of water molecules in the material.

Moreover dynamic effects (breakdowns and dark current) related to the high accelerating gradient have to be taken into account as well.

High accelerating gradient induces *breakdowns*, i.e. vacuum sparks which release a huge amount of energy creating craters on the surface. The high electric field, instead, induces field emission (*dark current*) which in turn cause Electrons Stimulated Desorption (ESD).

Only considering the geometry of the structure and the content of water, the pumping layout allows to have a background pressure of about $6 \cdot 10^{-9}$ *mbar* after

100 hours of pumping. This result fulfils the requirement set out by beam physics but the dynamic effect are missed in this discussion.
Breakdowns and dark current effects cause the release of physisorbed and chemisorbed molecules at the surface. The related rise of pressure causes beam loss and moreover it would not be detectable by the pressure gauges due to the local nature of the phenomenon, its short time scale and the narrow geometry of the accelerating structures.

Breakdowns measurement

For CLIC accelerating structure the requirement, for feasibility issue, is a breakdown probability of 10^{-7} $1/m$. The breakdown studies aim to find the material with the higher resistance to breakdowns.
The characteristic of the plasma between an anode and a cathode, inside a vacuum chamber, where a high electric field is applied, have been investigated developing a 1-D and 2-D Particle-In-Cell code[2]. Starting from the hypothesis that on the surface of the materials there are field emitter (tips, peak with higher roughness,..) from which electrons are emitted (cathode). The current flowing into the tips allows evaporation of metallic neutrals, due to the heating. The interaction with electrons leads to the ionization of this metal atoms, which once ionized are accelerated toward the surface of the cathode. This bombardment leads to a release of metallic neutrals and therefore to the self-sustained arcing process. In a RF accelerating structure the role of the cathode and anode are continuously switched and the whole structure acts as a cathode and as an anode almost at the same time.
As a support of RF tests, at CERN two DC spark experimental setups provide a cheap and effective alternative for breakdown studies.
The DC spark setup inside the vacuum chamber is shown in Figure 1.6: the cathode (i.e. the sample) is on the left side while the anode is cylindrical with spherical tip (on the right). The typical operation voltage ranges from 2 to 12 kV and thanks to the limited gap between the two electrodes (12 μm) it is possible to reach electric fields in the range of 100 to 800 MV/m. The measurement can be operated in two different mode: field emission mode and discharge mode (refer to Figure 1.7 for the electrical circuit). The first mode allowed to measure at which

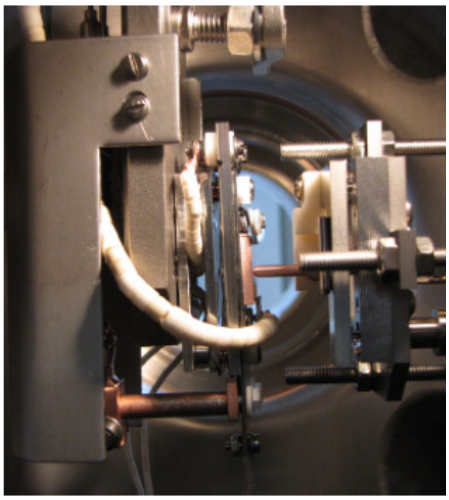

Figure 1.6: DC spark setup: cathode and anode

external electric field breakdown occurs. With the second method, instead, it is possible to extract the Breakdown Probability Rate (BPR), i.e. the numbers of breakdowns over the number of attempts, and the saturated field in conditioning mode. Moreover in one of the two setup a temperature controlled sample holder

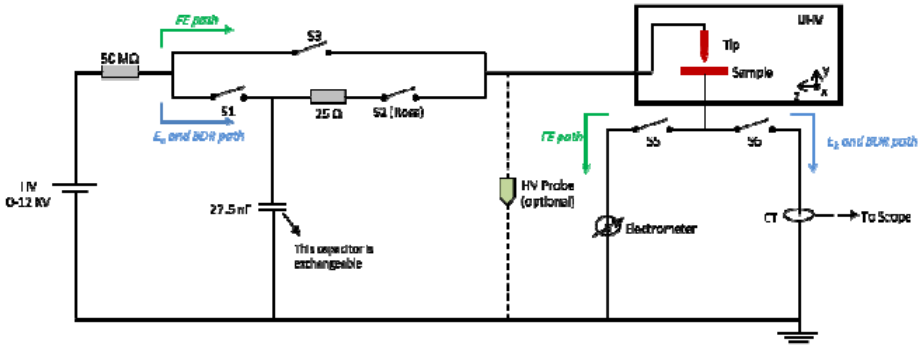

Figure 1.7: Schematic drawing of the electric circuit of the DC spark setup

is available which range from $-200°\ C$ to $1000°\ C$.
By means of this setup it is possible to test different materials, surface treatments and so on (more details in [3],[4],[5]).

Dark current studies

The high electric field inside the accelerating cavities induces field-emitted electrons. These electrons are then accelerated toward the surface of the cavities by the accelerating gradient induced desorption and therefore local burst of pressure. An estimate of the local increase of pressure was done by S. Calatroni using experimental data already available in literature. By means of a Faraday Cup the current related to field-emitted electrons in the accelerating structures have been measured. This analysis has been carried out using these dark current data and data, available from previous experiments, about the number of released molecules per impinging electron on copper surface.
The results showed a hydrogen partial pressure increase ten times higher than the limit value set by dynamics. Therefore it had been pointed out that further investigations were needed. This is the reason why the electron stimulated desorption measurement on the copper samples of the official campaign (refer to 1.3) was started two years ago.

1.3 Copper samples campaign for CLIC

For CLIC accelerating structures different production line have been designed.
The test accelerating structures produced up to know are diamond turned structures made of Oxygen Free Electronic grade copper. To produce the cavities a vertical bonding procedure is done starting from single elements as the one shown in Figure 1.8).
The cleaning procedures performed up to now are:

1. Simple degreasing without chemical etching (done at CERN)
2. Passivation treatment
3. Chemical etching according to SLAC (National Accelerator Center in Standford, California) procedures

After the cleaning of the diamond turned structures, the bonding cycle are done in a furnace for different atmospheres and thermal cycles. In particular the steps followed are almost the same (see Figure 2.6) but for different maximum temperature and atmospheres:

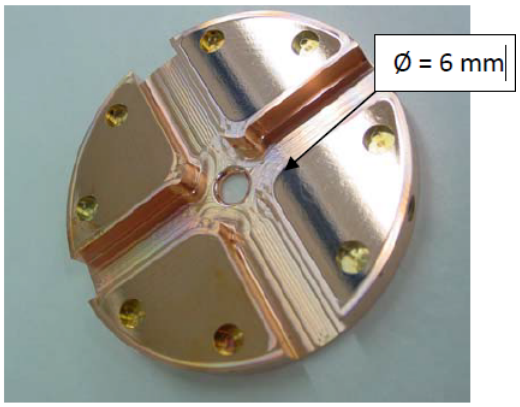

Figure 1.8: An element of the modular CLIC accelerating structure

1. Vacuum and $T_{max} = 790° \ C$

2. Argon at $P = 10 \ mbar$ and $T_{max} = 1040° \ C$

3. Hydrogen at $P = 10 \ mbar$ or $P = 1 \ bar$, $T_{max} = 1040° \ C$

Up to know the RF test on accelerating structures have shown that the bonding cycle for $P_{H_2} = 1 \ bar$ are the one which leads to better behaviour from the breakdown activity point of view.
However this is the worst treatment from physical-mechanical and economical point of view. Hydrogen, in fact, easily diffuse in the copper at high temperature contributing to embrittlement at copper grain boundaries as well as increase of gas content which can be released (e.g. for ESD) leading to local burst of pressure. Moreover handle hydrogen at such a pressure is an expensive and difficult technology.
In order to test each possible manufacturing procedure a combination of cleaning procedures and different thermal cycles with different atmospheres has been planned so that different samples are available to be tested. An overview of the samples campaign is given in Figure 1.9
These samples are usually tested with DC sparks test layout and ESD system (details in Chapter 3). The copper sample tested with laser ablation belongs to this samples campaign as well (details in Chapter 4).

	Vacuum			Argon (mbar)			HYDROGEN			H2 (1 bar)			Vacuum			Argon (mbar)			Hydrogen (mbar)			H2 (1 bar)		
	w/o etch	Passiv ation	SLAC etch	w/o etch	Passiv ation	SLAC etch	w/o etch	Passiv ation	SLAC etch	w/o etch	Passiv ation	SLAC etch	w/o etch	Passiv ation	SLAC etch	w/o etch	Passiv ation	SLAC etch	w/o etch	Passiv ation	SLAC etch	w/o etch	Passiv ation	SLAC etch
CERN	2	2	2										2	2	2	2	2	2						
Bodycote				2	2	2	2	2	2										2	2	2			
SLAC										2	2	2										2	2	4
	2	2	2	2	2	2	2	2	2	2	2	2	2	2	2	2	2	2	2	2	2	2	2	4

Figure 1.9: Samples campaign

1.4 Motivation and Tasks

In beam vacuum systems of accelerators the outgassing from the vacuum chamber walls and the induced desorption from the surfaces can strongly degrade the performance of the accelerator due to interaction of the beam with residual gas molecules. Therefore the background pressure and the residual gas composition have to fulfil strict requirements.
The design of CLIC accelerating structures and the high gradient applied on them have raised the problems of field emission and related local bursts of pressure. One of the phenomena induced by field emission is the Electron Stimulated Desorption from the surface of the copper cavities. Since hardly any literature is available on the Desorption Yield experimental data for unbaked copper and high energy electrons, a new ESD measurement system has been assembled here at CERN and the testing campaign has been started two years ago. The purpose of this work is to test samples with different chemical and heat treatment. Afterwards it would be possible cross-check the results of ESD measurement with the ones of breakdowns studies setups in order to choose the best treatment (refer to Chapter 3).
Hydrogen, which is typically the main gas component of Ultra-High-Vacuum (UHV) systems, is introduced in bigger quantity than usual in the modular accelerating structures of CLIC due to the manufacturing process(see section 1.3 for bonding cycles). During this process hydrogen is dissolved in the bulk of the material, rather than be concentrated at the surface.
To predict the outgassing behaviour of the materials, it is therefore necessary to determine the hydrogen content experimentally.
The idea of removing by laser ablation a know amount of material and measuring the released hydrogen quantity could be a suitable probe for the content measurement in copper samples.

Previous experiments on thin film coatings made it possible to measure argon content with an uncertainty of ±12%. These encouraging results gave the motivation to improve the setup and the measurement process in order to perform hydrogen content measurement in copper(refer to Chapter 4).

Chapter 2

Theory and models

The physical phenomena involved in the two main subject of this work are electron stimulated desorption and laser ablation of materials. In this chapter a brief introduction to the basic notions of these two wide topics will be discussed. In particular some Electron Stimulated Desorption (ESD) theoretical models and different regimes of laser-target interaction will be listed.

2.1 ESD: theoretical models

Electrons interaction with materials can induce the removal of atomic, molecular or ionic species from the surface.[6] This process is called Electron Stimulated Desorption (ESD) and is one of the fundamental mechanism of desorption and fragmentation induced by electronic transition at surfaces (photons and energetic particles as H^+ or He^+ can have the same effects) . The study of such processes is an important area in surface chemistry and physics, with many implications in basics science and technology. The scientific issues include the nature of chemical bonding at surfaces in both the ground and excited states, surface dynamical processes involving charge or energy transfer, interactions among adsorbates and the conversion of electronic potential energy into nuclear motion. Desorption induced by electronic transition (DIET) occur in almost every system involving the impact of energetic photons or charged particles on solid surfaces and is valuable for a variety of applications. For instance surface reactions can be controlled providing nonthermal energy by means of focused electron beams. The electron stimulated desorption ion angular distribution (ESDIAD)is uesd to determine bond direction-

ality. Moreover material growth, modification and pattering with this methods are an active research area. DIET process, however, can also be an unwanted side-effect in some surface analytical techniques such as photon-emission, Auger and electron-energy-loss spectroscopy, low-energy electron diffraction, etc.
The most important feature of ESD is that, as direct electron momentum transfer to the adparticle is negligible, electronic energy transfer must be considering to explain the ESD phenomenon and the energy of desorbed particles. In the next sections some ESD models will be discussed in chronological order.

2.1.1 The Menzel-Gomer-Redhead's model

Menzel, Gomer and Redhead proposed a general model of desorption via a sudden Franck-Condon electronic transition from the ground state to a repulsive state.[7][8] The transition is essentially instantaneous compared to time scale of nuclear motion. After this initial electronic excitation, the adsorbed species undergoes nuclear motion on the repulsive excited-state potential energy surface. Quenching of the excitation brings the adsorbate back to the ground state, and the electronic energy is converted into substrate excitation. Quenching can lead to either recapture of adsorbate or, if the kinetic energy is enough, to desorption. The ground-state desorption yield is determined by the cross section for the initial electronic excitation times the probability that sufficient kinetic energy will be gained on the excited-state curve before a quenching transition takes place. If no quenching transition occurs desorption along the excited-state curve is possible. Referring to Figure 2.1, the adparticle can experience one of the antibonding states (the repulsive and the excited states), where it can desorb as a neutral, or the ionic state where it can desorb as an ion.

After collected some ESD experimental data the evidence that the population of desorbed particles was mostly composed by neutral and not by ions were clear. Redhead completed the model explaining this preferential desorption channel. In case of an ionic primary excitation, an electron tunneling process can take place whilst the ion specie is desorbing from the surface the excited particle can be quenched and recaptured or it can desorbed as a neutral.
The MGR model is a very simple model and it does not specify the nature of the

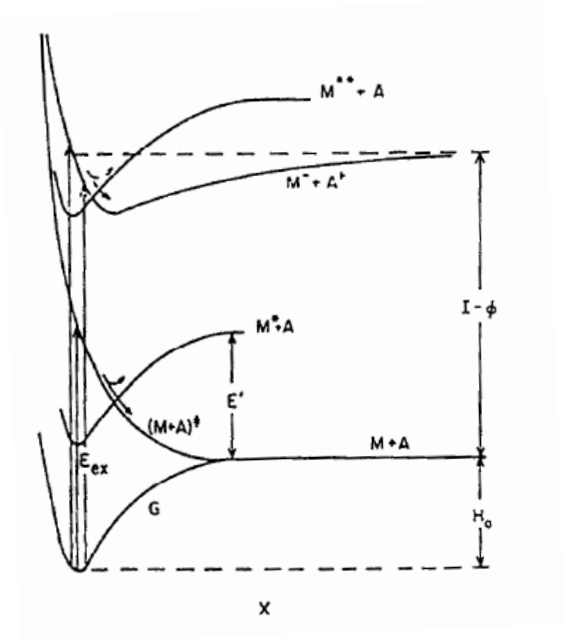

Figure 2.1: ESD mechanism proposed by MGR model

repulsive states and the relevant quenching processes.

2.1.2 The Antoniewicz's model

The basic problem Antoniewicz dealt with is the understanding of the process by which an ion or a neutral atom or molecule desorbs from a metal surface with an acquired energy of 10 eV or more.[9] The MGR model is based on a model for molecular dissociation, however there is evidence that excited states of atoms on a metal surface have a very short lifetime (of the order 10^{-16} s). There is a question as to the existence of a long-lived antibonding state.
The Antoniewicz model is based on a two step process: the excitation of the excited adsorbate-surface complex and the desorption sequence. The plausible desorption scenario starts with ionizing the adsorbed atom. With the ionic radius is smaller, and in some cases much smaller, than the atomic radius the Pauli repulsion is strongly reduced so, in combination with the image force which it experieces, the new equilibrium position it experience is considerably closer to the surface than the ground-state adsorbate equilibrium position. Therefore the ion starts moving

towards the surface. The ion neutralization can take place by resonance tunneling from the conduction band of the metal or by Auger neutralization. The first channel is represented by a vertical jump from the upper to the lower curve in Figure 2.2.

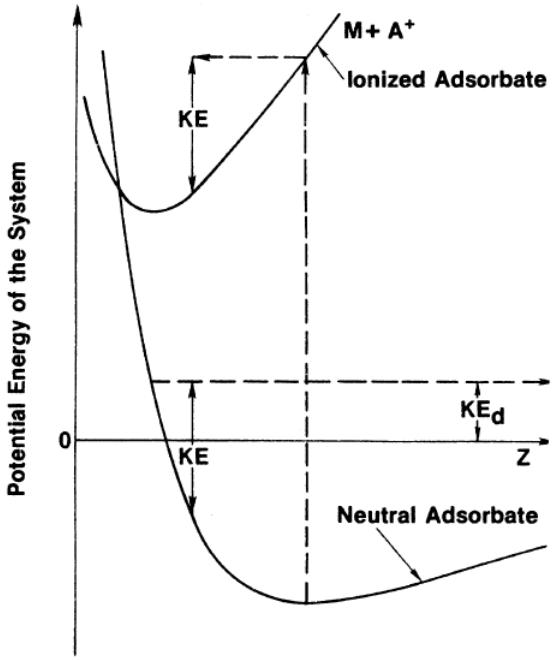

Figure 2.2: Antoniewicz's model for desorption of neutrals

To have a neutral desorb from state 2 the ion has to move towards the surface sufficiently so that its kinetic energy plus the ground-state potential energy exceed the binding energy of the neutral atom:

$$[V_2(z_0) - V_2(z_n)] + V_0(z_n) \geq 0 \tag{2.1}$$

where V_2 is the potential energy of the excited state, V_0 the potential energy of the ground-state and z_0 the equilibrium position for the ground-state (we assume that the atom is initially at rest). Let's z_d be the distance at which (2.1) is zero and z_n the distance at which the ion is neutralized, then the neutral atom will desorb if $z_n < z_d$ otherwise the particle will remain trapped at the surface with the surface bond excited.

The desorption process for ions is more complicated and require at least two tunneling processes to occur. The initial state with the lowest threshold energy, is an excited positive ion on the surface referred to as V_2 in Figure 2.3. The excited ion moving towards the surface, must be neutralized sufficiently close to the surface to be high up on curve V_0 and then be ionized again by electron tunneling to the surface and find itself on curve V_1 before it leaves the close vicinity of the surface. V_1 is the ground-state-ion-potential-energy curve. In this simplified model the energy levels of the atom are assumed not be broadened by the interaction with the surface and the energy losses of the ions due to interaction with the surface are also not considered.

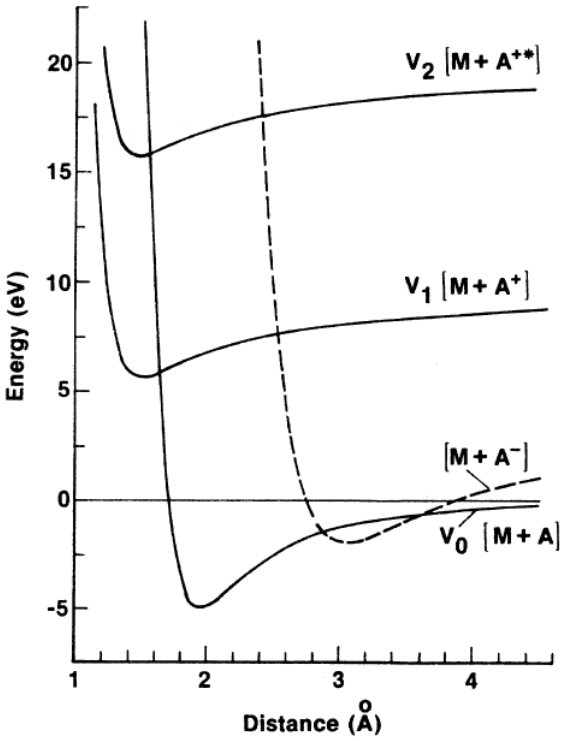

Figure 2.3: Antoniewicz's model for desorption of ions

If the neutalized particle has sufficient total energy, then can be reionized:

$$V_2(z_0) - V_2(z_n) + V_0(z_n) \geq V_1(z_n) \tag{2.2}$$

For the particle to desorb as an ion, it has to be neutralized in the region $z_2 < z_n < z_1$,

where z_1 is the solution of the (2.2) for the equal sign and z_2 is the solution of the equation $V_2(z_2) = V_0(z_2)$. This model agrees qualitatively to experimental data and predicts the presence of high-energy neutrals desorbing along with the ions and negative-ion desorption from the same initial excited state. It has to be pointed out that the desorption probabilities depend very sensitively on the shape and positions of the potential energy curves relative to each other and the Fermi level and where on the curve the ion starts its motion. This agree with the observed sensitivity of the desorption cross section on the adsorption sites and temperature.

2.1.3 The Gortel's model

The attempts to find an agreement between theoretical result of Antoniewicz model and experimental observations have been unsuccessful.[10] The common problem is the inability of accounting simultaneously for the total desorption yield and for the kinetic energy distribution of desorbing neutral particles. Therefore, at least for the physisorbed system for which enough ESD experimental data exist, no conceivable modifications of the standard desorption scenario would ever be able to account for the observed behaviour.
The scenario of desorption proposed by Gortel is called Wave Packet Squeezing (WPS) and will be briefly discuss hereafter. As a result of the initial excitation sequence the system is promoted to the electronic state in which the atom is bound to the surface by a potential V_d which is narrower and deeper than the ground state potential is but has nearly the same equilibrium position. The system evolves in this potential until an electronic deexcitation process returns it to the electronic ground state. In order to have a closer look at the kinetic energy gain from the quantum mechanical point of view, let's consider a one-dimensional model, considering the momentum operator p one can write:

$$E_{kin}(t) = \frac{1}{2m}[<p(t)>^2 + (\Delta p(t))^2] \tag{2.3}$$

where the first term on the r.h.s. is the expected kinetic energy of the particle at time t in the state described by the wave packet $\Psi(z,t)$ and $\Delta p(t)$ is the quantum fluctuation of momentum. According to Ehrenfest theorem $<p(t)>$ satisfies the ordinary Newton equation so the first term on r.h.s. of (2.3) is the classical con-

tribution to the kinetic energy $[V_d(z_0) - V_d(<z(t)>)]$ present already in (2.1).
At low enough temperature the adsorbed particle before the initial excitation is described by the ground state wave function of the ground state potential $V_0(z)$ with $<p(t=0)> = 0$ and $<z(t=0)> = z_0$. This is the minimum uncertainty wave packet for this potential and in the usual MGR picture is placed on a smooth part of $V_d(z)$. In the initial stages of its time evolution its center $<z(t)>$ accelerates towards the new equilibrium position, the time evolution of $<p(t)>$ is governed by classical mechanics, and the position uncertainty $\Delta z(t)$., which is related to the momentum uncertainty by Heisenberg equality $\Delta p(0)\Delta z(0) \approx \hbar/2$ increase(familiar wave packet spreading).
The situation changes in the WPS scenario. Let's consider a somewhat extreme case in which the equilibrium positions of $V_0(z)$ and $V_d(0)$ coincide exactly. Both potentials are shown in Figure 2.4: the ground state potential is chosen as the Morse potential of depth V_0, the wave packet evolving from the ground state is too tight for it. The center of the packet remains at rest, so $<z(t)> = z_0$,$<p(t)> = 0$ but $\Delta z(t)$ decreases as show in Figure 2.4for three instants of time (displaced vertically to avoid overlapping).The initial wave packet is already the minimum uncertainty wave packet so, in order to satisfy the Heisenberg uncertainty principle, $\Delta p(t)$ must increase. In this extreme case, only the second term of (2.3) contributes to kinetic energy gain. If the gain exceeds the binding energy V_0at $z = z_0$ then the particle desorbs. More generally, approximate condition for desorption particle deexcited at an instant t can still be written in the form of somewhat modified inequality (2.1):

$$\mathcal{E} = V_d(z_0) - V_d(<z(t)>) + \frac{1}{2m}[(\Delta p(t))^2 - (\Delta p(0))^2] + V_0(<z(t)>)>0 \qquad (2.4)$$

It is not easy to estimate $\Delta p(t)$ without actually solving the time-dependent Schrödinger equation so the usefulness of the above formula is rather limited. Detailed calculation of yields and kinetic energy distribuitions requires finding on overlap between the time dependent wave packet an the continuum wave function corresponding to $\mathcal{E} = \hbar^2 q^2/2m$ of the detected particle.
For instance in Figure 2.5experimental (crosses) and theoretical results in the WPS model (solid curve) for the kinetic energy distribution of Ar atoms desorbing from Ru are shown. To be noticed the strong agreement.

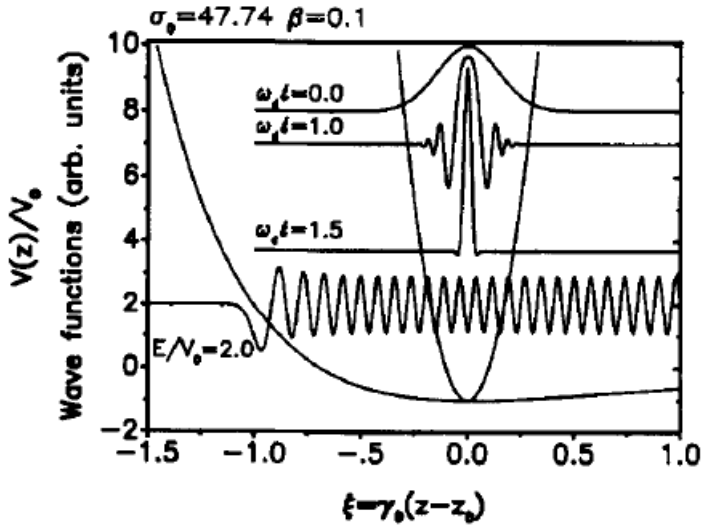

Figure 2.4: Surface potential for the extreme WPS scenario with coincident equilibrium positions.

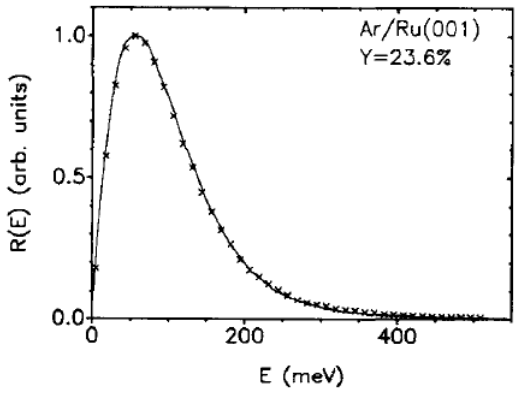

Figure 2.5: Experimental and theoretical result comparison, Ar atoms desorbing from Ru (0 0 1)

2.2 Laser Ablation: a brief introduction

There are several regimes characterizing laser-target interaction which depend on laser intensity, wavelength and pulse duration. It's well known that powerful laser irradiation alter optical properties (commonly related to dielectric function, refractive index, absorption coefficient) of many materials and often drastically so. Moreover beam-target coupling can induce phase transitions and affect shape of the irradiated materials (e.g. undesired surface corrugation but can also be used for controlled hole drilling).

For irradiance above 10^3 W/cm^2 evaporation is achieved[21]. At relative moderate irradiance (below $\simeq 10^6$ W/cm^2) the vapor is tenous and essentially transparent, but with increasing irradiance it tends to become supersaturated as it evolves from the surface. Condensing droplets of submicrometer size then lead to absorption and scattering. Apart from this, the vapour cloud is a medium of refractive index different from its surroundings and distorts the incident wavefront. Between roughly 10^7 and 10^{10} W/cm^2, depending on wavelength, the vapour becomes partially ionized and absorbs a substantial fraction of the laser energy. On the other hand, blackbody radiation emitted by the vapour plasma tends to be absorbed by the solid more efficiently than the laser radiation. If the plasma stays close to the surface, it may actually enhance the fraction of beam energy absorbed in the solid. At irradiance somewhat higher than those producing ionization of the hot vapour, ionization may even occur in the cold ambient gas, due to optical breakdown. The breakdown plasma typically propagated as a supersonic absorption wave against the incident beam and shields the material completely. At even higher irradiance (above $10^9 \div 10^{10} W/cm^2$) the plasma, owing to its high temperature, becomes transparent and light is again transmitted to dense surface. The ablation pressure drives a shock wave into the material which may alter its optical properties. Finally, at highest irradiance ($\geq 10^{15}$ W/cm^2)any sharp boundary between the condensed material and the plasma disappears. Light is absorbed at that surface where the electron density makes the plasma frequency equal to the laser frequency, additional absorption and reduced reflectance arises in the plasma from turbulent collective motion of the electrons.

2.2.1 Evaporation and plasma generation

One of the most prominent features in laser ablation with nanosecond pulses lasers for UV wavelength is the ionization of laser-ablated vapours leading to the plasma generation. A very simplified physical explanation of this phenomenon will be given in the this section.[22]

When a solid target is irradiated by intense laser beam the incident laser radiation penetrates the target and induces the oscillations of the electrons in the target media. The electrons gain energy from the oscillating field through the phase disruption due to random collisions with atoms. The electron oscillation energy converts to electron excitation and electron kinetic energy.
An increase in the electron energy leads to ionization of the target at the solid-vapour boundary and the formation of a dense plasma by *photoionization*, *multi-photon ionization* and *ionization by electron impact*. The process of optical breakdown and plasma formation is due to avalanche ionization for IR and visible wavelength and multiphoton ionization for UV wavelength lasers.

Multiphoton ionization

The multiphoton ionization is a threshold-free process and for moderate intensity ($I = 10^8 \div 10^9\ W/cm^2$) is responsible of the creation of seed electrons in the plume. These electrons are accelerated in the laser field and result in avalanche ionization by electron impact to form laser-produced plasma. The probability of multiphoton ionization W_{mph} by absorbing n_{ph} laser photons to strip an electron with ionization potential $J_i$can be expressed by the formula:

$$W_{mph} \approx \omega_0 n_{ph}^{\frac{3}{2}} \left[1.36 \frac{\varepsilon_{osc}}{J_i}\right]^{n_{ph}} \tag{2.5}$$

where

$$\varepsilon_{osc} = \frac{e^2}{16\pi\epsilon_0 m\pi c^3} I\lambda^2 \tag{2.6}$$

is the oscillation energy of an electron in the field of the laser electromagnetic wave with the frequency ω_0 and wavelength λ; c is the speed of light in vacuum and ϵ_o is the vacuum permittivity. The number of photons n_{ph} needed to strip off an

electrons is equal to the integer part of the quantity:

$$n_{ph} = \frac{J_i + \varepsilon_{osc}}{\hbar\omega_0} + 1 \tag{2.7}$$

As the laser wavelength decrease, the number of photons needed to ionize the vapour decrease and the ionization probability increase.

Acceleration of electron in the laser field

The energy of an electron accelerated by the laser electric field can be calculated as

$$\frac{d\varepsilon_e}{dt} = \Delta\varepsilon\nu_{ea} \tag{2.8}$$

where

$$\Delta\varepsilon = \frac{2\varepsilon_{osc}\omega_0^2}{\omega_0^2 + \nu_{ea}^2} \tag{2.9}$$

is the average energy gained by an electron as a result of a single collision and ν_{ea} is the average over the electron spectrum collision frequency between electrons and atoms in the target, which can be determined for the particular target material with the help of the Boltzmann transport equation for the entire range of electron energies. As a reasonable estimate for the collisional frequency is $\nu_{ea} \simeq 10^{14}$, one can conclude that the average energy gain per collision is approximately $2\varepsilon_{osc}$. Hence it follows that, for a given laser intensity and collisional frequency, the electron energy decrease with the decreasing wavelength: $\varepsilon_e \propto I\lambda^2$. An other important parameter is the time t_{ion} required for electron to gain an energy equal to the ionization potential:

$$t_{ion} \simeq \frac{J_i}{\Delta\varepsilon\nu_{ea}} \tag{2.10}$$

Threshold conditions for optical breakdown

Ionization by electron impact is the most efficient ionization mechanism in solids and in a dense gas (atomic number density bigger than $10^{18}\ cm^{-3}$). This mechanism is also responsible for optical breakdown of the vapour and consequently

for the vapour-to-plasma transition. The initial free electrons created by multi-photon ionization or presented in the target as free carriers, are accelerated in the laser field and result in avalanche ionization by electron impact to form the laser-produced plasma. Electron avalanche during the laser pulse duration t_p may produce a total density of electrons n_e:

$$n_e = n_{e0} e^{\frac{t_p}{t_{ion}}} \tag{2.11}$$

where n_{e0} is the density of seed electrons produced by photoionization and multiphoton ionization or the free carrier density, whichever is larger. The condition for optical breakdown is taken to occur when the number density of the produced electrons equals the critical density for the appropriate laser wavelength. The critical plasma density n_c is the density where the electron plasma frequency equals the frequency of the laser radiations ω_0 ; this is the maximum plasma density the laser wave can penetrate.

$$n_c[cm^{-3}] = \frac{4\pi\epsilon_0^2 m_e \omega_0^2}{e^2} \tag{2.12}$$

When the electrons density n_e exceeds the critical density the vapour are not transparent any more and the laser energy goes into the plasma. The avalanche ionizations includes several processes: electrons gain energy in the laser field, then further electrons are generated in electron-atom collision, some of the produced electrons diffuse out of the laser interaction area and some recombine into atoms due to electron-ion inelastic collisions. In most of the case the recombination losses are negligible both in solid target and the atomic vapour and the time required to ionization is much lower than the diffusion time, so it's possible to express the condition for optical breakdown of the vapour with a "rule of thumb"(combination of (2.6),(2.10),(2.11)):

$$t_p \times \lambda^2 \times I = C \tag{2.13}$$

where C is a constant depending on the material ablated. The laser intensity, wavelength and pulse duration are the key parameters of the laser-target interaction, allowing or not the dielectric breakdown in the vapour and the plasma generation.

Other mechanisms related to skin-effect may induce plasma for intensity below the threshold condition discussed so far, but the explanation of these goes beyond the scope of this discussion.

An experimental investigation of the *plasma threshold* requires a probe capable of monitoring the transition from thermodynamic to the plasma region: spectroscopy of the plasma fluorescence and detection of charged particles are both suited, but also some different set-up as acoustic mirage effect technique have been used during these years. In this work results from detection of electrons will be shown and compared with the data available in the literature.

2.3 Hydrogen solubility in Copper and other materials

Previous calculations have been done to estimate the hydrogen content introduced inside the copper during the bonding cycle introduced in section 1.3. In particular the phenomenon involved is temperature induced diffusion of molecular hydrogen in copper. To understand a little bit more it is necessary to introduce the concept of solubility of atomic hydrogen in a solid structure. Firstly the hydrogen molecules should dissolve in atoms at the solid surface following the endothermic reaction:

$$M + \frac{x}{2}H_2 \rightarrow MH_x + x\Delta H_{sol} \tag{2.14}$$

where x is the number of moles of hydrogen and ΔH_{sol} is the solution enthalpy per mole. At the equilibrium the chemical potentials of molecular hydrogen in the gaseous atmosphere and the hydrogen dissolved in copper must be equal:

$$\mu_H = \frac{1}{2}\mu_{H_2} = \mu_{H_{gas}} \tag{2.15}$$

Therefore considering the chemical potential of an ideal gaseous phase and the Sievert's law, it's possible to write:

$$\mu_H = \mu^0_{H_{gas}} + RTlnP_{H_2} = \mu^0_{H_{gas}} + RTln(s \cdot {\chi_H}^2) \tag{2.16}$$

$$\mu_H - \mu^0_{gas} = RTlns + 2RTln\chi_H \tag{2.17}$$

where P_{H_2} is the hydrogen partial pressure at copper surface, s is the Sievert's law constant and χ is the solubility.
Introducing the definition of Gibbs free energy (S is the entropy), the previous equations become:

$$\mu_H - \mu^0_{gas} = \Delta G = \Delta H_{sol} - TS_{sol} \tag{2.18}$$

$$ln\chi_H = \frac{\Delta H_{sol}}{2RT} - \frac{S_{sol}}{2R} - \frac{lns}{2} \tag{2.19}$$

$$ln\chi_H = \frac{\Delta H_{sol}}{2RT} + \frac{lnP_{H_2}}{2} - \frac{lns}{2} \tag{2.20}$$

where ΔH_{sol} is the solution enthalpy defined in (2.14).
To estimate the hydrogen solubility in materials empirical formulas are available for specific range of temperature and hydrogen partial pressure. In the case of copper the formula is [11]:

$$log\chi_H = \frac{1}{2}logP_{H_2} - 4.77 - \frac{2426}{T} \tag{2.21}$$

which is valid for $770 \div 1356K$ and P_{H_2}<10^5. The third term in the right-end-side of eq2.21 is the solution enthalpy H_{sol} and the fact that is negative means that the dissolution of hydrogen in copper leads to an increase of the energy of the system. It has to be noted that the solubility increase with the pressure and temperature.

2.3.1 Diffusion of hydrogen in copper

For simplified geometries the concentration of diffusing element C is describe by the 1-D Fick's law:

$$\frac{\delta C}{\delta t} = D\frac{\delta^2 C}{\delta^2 x} \tag{2.22}$$

The diffusion coefficient D is typically defined by the exponential equation:

$$D = D_0 e^{-\frac{E}{RT}} \tag{2.23}$$

where E is the activation energy for the diffusion and T is the temperature, which acts as a boost for the diffusion. Empirical formula are also available for calculate the diffusion coefficient for particular gas-metals system at a certain temperature.[11] Let's consider as a first approximation of the copper sample a plane sheet of thickness l, with these initial and boundary conditions:

$$C = \begin{cases} 0 & t = 0, 0 < x < l \\ C_s & t \geq 0, x = 0 \\ C_s t & t \geq 0, x = l \end{cases}$$

where C_s is the solubility of hydrogen in copper for a certain temperature and gas pressure.
Considering the bonding cycle in Figure 2.6 (more details in Chapter 1), the hydrogen diffusion profile at the end of the bonding plateau and at the end of the

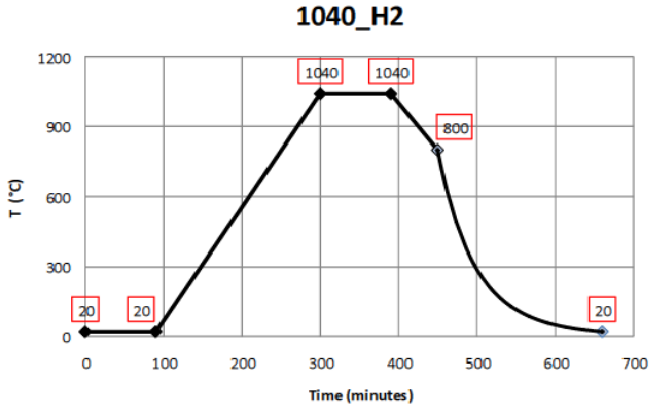

Figure 2.6: Bonding cycle for treatment at 1 bar of Hydrogen

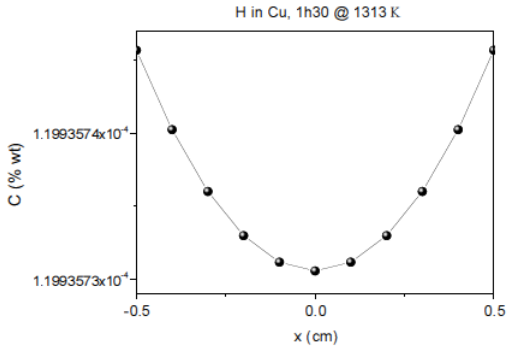

Figure 2.7: Hydrogen diffusion profile at the end of the bonding plateau

thermal ramp down have been calculated approximatively. The results shown in Figure 2.7 and Figure 2.8:

Note that the content of hydrogen (expressed in weight percent in the graph) is almost equal to the solubility and that the maximum is reached at the surfaces and the minimum at the mirror plane. Most important feature: the concentration profile change only by 1 ppm.

For this calculation the ramp down has been approximated by a step function (each step as a decreasing temperature by $4°C$ and lasts 60 seconds) updating for each step the initial condition with the diffusion profile calculated in the previous step. The diffusion profile is minimum at the surfaces: while the temperature

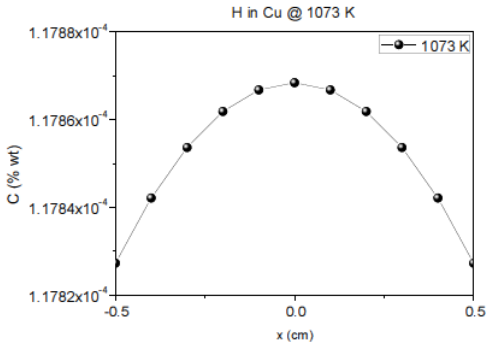

Figure 2.8: Hydrogen profile at the end of the thermal ramp down

decrease the copper release a certain amount of hydrogen. After the thermal ramp down the bonding cycle lasts with the annealing of the structure for 10 days under $650°C$ but as the diffusion at lower temperature is a slower process the diffusion profile is not expected to change a lot.
In conclusion the amount of atomic hydrogen in materials is limited by the solubility of hydrogen at the particular pressure and temperature of the treatment they have been subjected.
In Table 2.1 are shown the solubility value related to the samples tested (copper for both ESD and ablation, titanium only for ablation) calculated with empirical formulas [11][12].

Copper	76 ppm	$T = 1040C°$	$P_{H_2} = 1\ bar$
Titanium	4.75 10^4 ppm	$T = 1020C°$	$P_{H_2} = 15\ mbar$

Table 2.1: Hydrogen solubility values for tested samples

The titanium has been taken into account for its huge solubility as a reference to test the measurement process itself, in particular two different samples have been used one with expected content of 4.7510^4 ppm and one not subjected to thermal treatment.

Chapter 3

ESD of OFE Copper: Desorption Yield measurement

The need to estimate the desorption induced by electrons of high energy on OFE-Oxygen Free Electronic grade copper samples has been already pointed out in Chapter 1. Models discussed in section 2.1 can help understanding the physical background of ESD (Electron Stimulated Desorption), in this chapter the experimental process used to quantify this phenomen is discussed.
The ESD is usually described referring to Desorption Yield. This parameter allows to compare the behaviour of different materials and can be calculated from experimental data.

3.1 Calculation of the Desorption Yield

Considering a vacuum chamber of volume V in thermal equilibrium: the temperature T and the pressure p are constant over the whole volume. Starting from this hypothesis is possible to write the ideal gas law:

$$pV = Nk_BT \tag{3.1}$$

where $k_B = 1.38\ 10^{-23}\ J/K$ is the Boltzmann constant and N is the number of particles inside the system. A target bombarded by electrons within the system leads to a pressure rise Δp.
The number of particles which are desorbed from the target can be calculated by:

$$N_{des} = \frac{\Delta p \cdot V}{k_B \cdot T} \tag{3.2}$$

The ESD yield η is then:

$$\eta = \frac{N_{des}}{N_{elec}} = \frac{\Delta p \cdot V}{N_{elec} \cdot k_B \cdot T} \tag{3.3}$$

This is valid as long as the volumetric flow rate of the pumping system (the pumping speed S) is neglected.
The gas flow rate $\dot{Q}$, expressed in $m^3 \cdot Pa/s$, is defined as:

$$\dot{Q} = \frac{d(p \cdot V)}{dt} \tag{3.4}$$

Considering a real vacuum chamber, one has to take into account all the different gas flow rate contributions.
If the transformation of species, e.g. chemical reaction products, can be neglected it is possible to write the following equilibrium equation:

$$\dot{Q}_{vol} + \dot{Q}_{des} - \dot{Q}_{pump} = 0 \tag{3.5}$$

where $\dot{Q}_{vol}$ is the gas load of the chamber (due mostly to the outgassing of the system walls), $\dot{Q}_{des}$ is the gas load due to the desorption and the third term is the gas load pumped down by the pump.
The (3.5) is valid for each gas species inside the chamber:

$$\left(-\frac{\delta p_j}{\delta t} \cdot V\right)_{vol} + \left(\frac{\delta p_j}{\delta t} \cdot V\right)_{des} - p_j S_j = 0 \tag{3.6}$$

and more:

$$\left(\frac{\delta p_j}{\delta t} \cdot V\right)_{des} - p_j S_j = \left(\frac{\delta p_j}{\delta t} \cdot V\right)_{vol} \tag{3.7}$$

where S_j is the pumping speed of the gas species j and the minus sign in the first term of (3.6) is due to the fact that as long as the system is pumped down, the gas load of the volume is decreasing over time.
In steady state condition the gas load of the chamber is in equilibrium with the pumping system, therefore the (3.7) becomes:

$$\left(\frac{\delta p_j}{\delta t} \cdot V\right)_{des} = p_j S_j \tag{3.8}$$

which states that each gas species, produced during the pressure burst due to electrons impinging on the surface, is pumped by the pumping system with a different pumping speed.
Differentiating (3.3) and considering (3.8), one has:

$$\left(p_j^1 - p_j^0\right) S_j = \eta_j \frac{I_s}{e} kT \tag{3.9}$$

where p_j^0 is the background pressure of the system reached in steady state condition and the p_j^1 is the pressure burst due to the desorption. I_s is the electrons current bombarding the surface expressed in [Ampère] and $e \approx 1.602\ 10^{-19}\ C$ is the elementary charge, therefore I_s/e is the number of electrons bombarding the surface per unit time.

The desorption yield η_j, expressed in [desorbed molecules/electron], is then:

$$\eta_j = \frac{(p_j^1 - p_j^0) S_j}{\frac{I_s}{e} kT} \tag{3.10}$$

3.2 Experimental Setup

In literature, desorption yield data from previous experiments are available but considering the framework of CLIC study they are only partially useful. Unbaked copper samples have been already tested at CERN but with 0.35 keV electrons as well as baked copper samples for higher electron energies. Therefore, to our knowledge, there was a leak of data for unbaked copper and high electron energies. The experimental set-up, described hereafter, has been assembled to operate with 10 keV electrons and unbaked copper samples. This energy is still not comparable to the expected electron energies in the working condition of CLIC accelerating structures, but it is two orders of magnitude higher than the conditions of available data.
The lay-out of ESD experimental system is shown in Figure 3.1 and the components are highlighted in Figure 3.2.
The system is divided into two chambers by means of a butterfly valve: the upper chamber (volume$\approx$ 1.5 $liters$) and the lower chamber (volume$\approx$ 2.9 l). Each vacuum chamber is connected to a pumping system made up of one primary pump

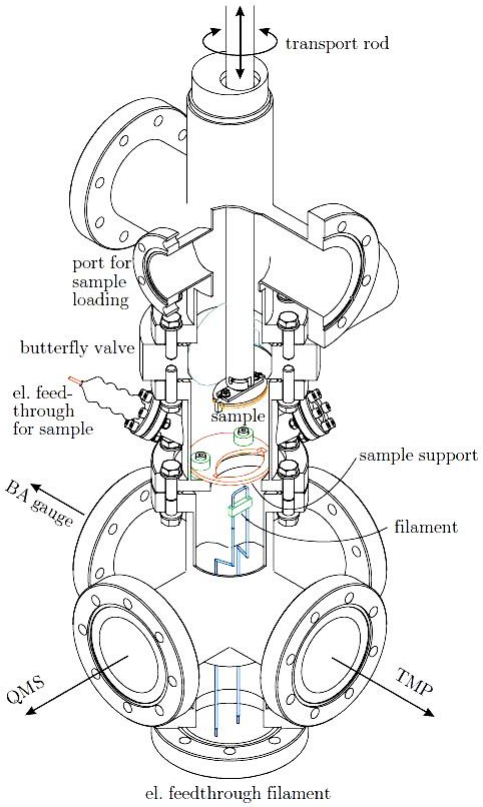

Figure 3.1: Vacuum system lay-out

and one turbomolecular pump (TMP). On the upper chamber there are the connections for the transport rod and a lateral blind flange by means of which the sample is inserted into the system.
The Residual Gas Analyzer (RGA), the Bayard-Alpert gauge and a full range gauge (Pirani + Penning gauge) are connected to the lower chamber. The injection line, used for calibration of RGA, is linked to the bottom of the lower chamber. To measure small pressure increases, a small orifice acting as a conductance reducing the pumping speed in the lower chamber was used (more details in section 3.3.1).
The presence of two different chambers is needed in order to do not bake-out the sample. The bake-out, which is an artificial acceleration of the process of outgassing by means of heating procedure, is needed to reach a background pressure around 10^{-9} *mbar*. Therefore just the lower chamber is baked while the sample is

holding in the upper one.
When the lateral blind flange is opened to insert the sample into the system and during the pump down of the upper chamber, the butterfly valve is closed to keep the pressure low in the lower chamber. Afterwards the sample is loaded on the sample support by means of the transport rod. The transport rod is manipulated magnetically , therefore the positioning of the sample on the sample holder is easy, fast and leaks in the vacuum system are avoided. The butterfly valve is a manual operated valve to prevent sudden closing of the valve for instance during power cut.
The RGA records the partial pressures of different gas species over time, while the full range gauge is used to monitor the total pressure. The Bayard-Alpert (B-A) is used to calibrate the RGA. The injection line, usually connected with hydrogen and nitrogen bottles, is provided with a cold trap and a primary pump to pre-

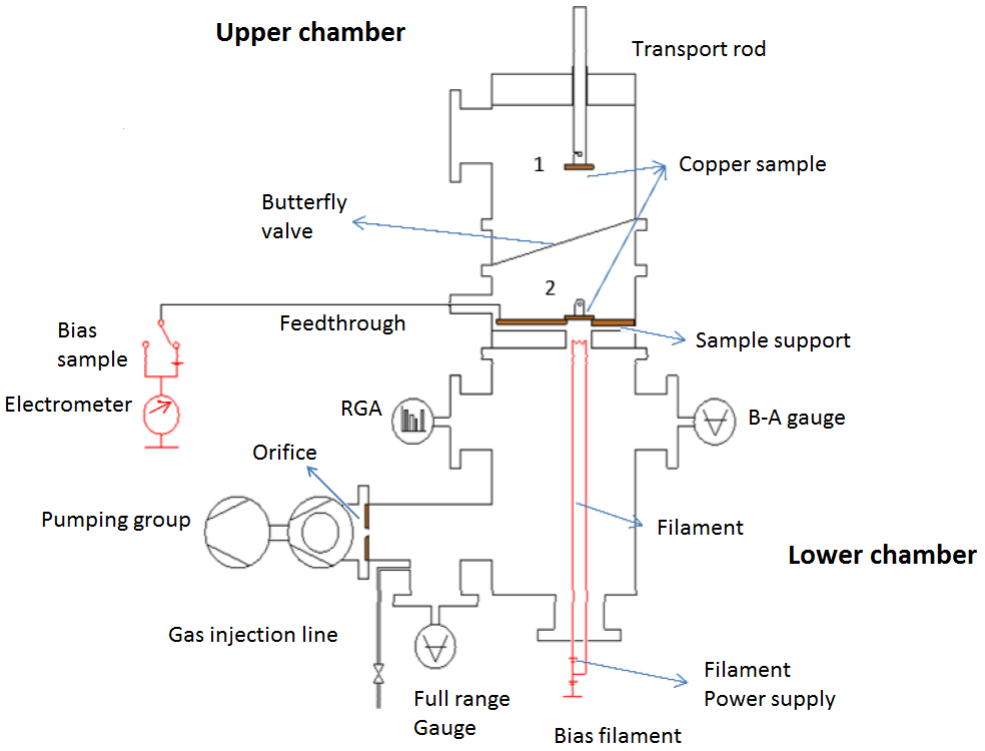

Figure 3.2: Highlight of main components of vacuum system

vent the contamination of the chambers during the RGA calibration process. The gauges and the RGA are described in details hereafter.

A tungsten filament acts as an electron source. The filament, normally operated at $2 \div 3$ A and $4 \div 9$ W, emits electrons by thermoionic effect. The sample holder, and thus the sample, can be positively polarized up to 20 kV . The power supply which operate the bias can reach 35 KV but the voltage is limited by the vacuum electrical power feedthrough.
Referring to the electrical circuit in Figure 3.3 one can see that two electrometers are connected to the system: the one connected to the filament reads the electrons emitted by thermoionic effect and the other, connected to the power feedthrough, measures the electronic current impinging on the sample. Therefore, if no other electron sources apart from the filament are in the system, these two currents have to be equal since all the electrons emitted are accelerated towards the sample.
The filament is slightly positively biased to the ground in order to trap electrons when the sample is not biased. If the emitted electrons are not attracted by a positive bias they can go toward the wall of the system and in turn cause ESD. This would increase the background pressure and decrease the accuracy of the measurement.

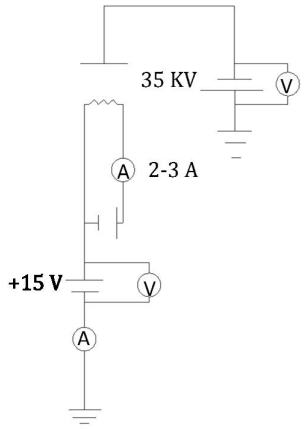

Figure 3.3: Electrical circuit of ESD measurement system

Pirani gauge

The operating principle of a Pirani gauge is the thermal conductivity of gases at pressures less than 1 $mbar$. A filament (usually tungsten) within a tube is electrically heated to a constant temperature between 110° C and 130° C by passing a current through it (see the schematic drawn in Figure 3.4). The surrounding gas dissipates the heat to the wall of the tube. In the molecular flow range, the thermal transfer is proportional to the molecular number density and thus to the pressure. Therefore, if the temperature of the filament, which is found from its resistance, is kept constant, its heat output will be a function of pressure.
However it will not be a linear function of pressure, as the thermal conduction (C) to wire supports and thermal radiation (R) will also influence the heat output (refer to Figure 3.5). The total energy loss rate W_T is therefore given by:

$$W_T = W_R + W_C + W_G \tag{3.11}$$

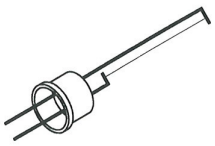

Figure 3.4: Pirani gauge

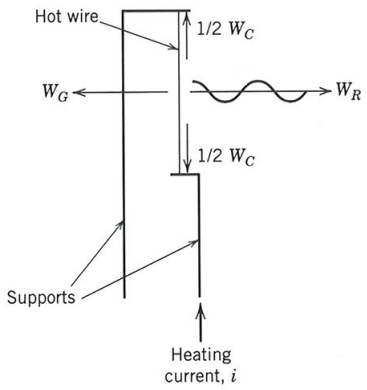

Figure 3.5: Energy loss mechanism of heated wire in a gas at reduced pressure

It is possible to examine the functional dependences of each term referring to an incremental length dl of a long wire of diameter D_1, emissivity ϵ_1 and temperature T_1 located in a long cylinder of radius r_2, emissivity ϵ_2 and temperature T_2.
Assuming $r_2 \gg D_1$ and $T_1 > T_2$, the rate of energy transfer by radiation is:

$$W_R = \epsilon_1 \sigma (T_1^4 - T_2^4) 2\pi D_1 \, dl \tag{3.12}$$

where σ is the Stefan-Boltzmann constant. Therefore it is desirable, in gauge design, to choose a sensor wire with a low and stable emissivity.
Assuming the same situation at each end, the energy transfer rate by conduction to the cooler support along the wire is:

$$\frac{1}{2} W_C(l) = G \, \pi r_1^2 \frac{dT_l}{dl} \tag{3.13}$$

where G is the thermal conductivity of the material of the wire. This contribution to the heat loss can be reduced by using a long wire of small diameter.
For the case when the mean free path of molecules is greater than $r_2 - D_1$, i.e. molecular flow condition, the heat transfer between coaxial cylinders has been studied. It is possible assume that the gas molecules have a Maxwellian energy distribution corresponding to T_2 and a probability α to land on the surface and depart with an energy distribution corresponding to T_1. Then the heat transfer rate by gas molecules is:

$$W_G = \frac{1}{4} \frac{(\gamma + 1)}{(\gamma - 1)} \alpha \sqrt{\frac{2k}{\pi m T_2}} (T_1 - T_2) p \tag{3.14}$$

where $\gamma = C_p / C_v$ is the ratio of specific heats of the gas, m is the mass of a gas molecule and k is the Boltzmann constant.
The region of linear behaviour of W_G with p extends to about 1 bar for nitrogen, while for other gases there are significant deviations. In Figure 3.6) the indicated pressure over the actual pressure is shown for different gases.
This deviation from linear trend starts when energetic molecules departing from the filament collide with other molecules before getting far from the wire acting as a sheath of hot gas near the wire. Therefore there is no more effective heat transfer until the onset of convection. The lower limit of Pirani gauge measurement range is due to the predominant heat transfer to the ends over the conductivity of gas and is found at 10^{-4} $mbar$.

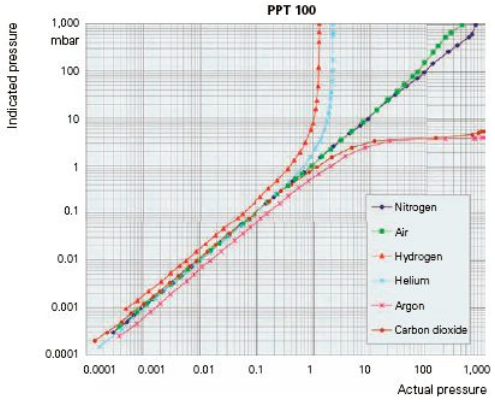

Figure 3.6: Pirani gauge: indicated pressure over actual pressure for different gas species

IONIZATION GAUGES

Ionization gauges cover a wide range of pressure measurement: $10^{-14} \div 10^{-3}\ mbar$. The generalized lay-out of an ionization gauge is shown in Figure 3.7. The ionizing particles (usually electrons from a thermionic source) enter the ionizing space containing gas molecules (drawn as circles) at reduced pressure. The electrons induce ionization of molecules which are afterwards collected on the suitably biased electrode. The electrometer then records the ion current as an indirect measure of gas pressure.

Hot-cathode gauge: Bayard-Alpert gauge

The design of a Bayard-Alpert (B-A) is shown in Figure 3.8. The source of electrons is one (or more) heated filament (cathode). A wire is arranged in the middle of a cylindrical anode and it acts as the ions collector. A voltage of approximately 100 V applied between anode and cathode accelerates the electrons toward the former. The electrons have enough energy for ionization over a portion of their path and the ions are then accelerated towards the collector which is at the same potential of the cathode.

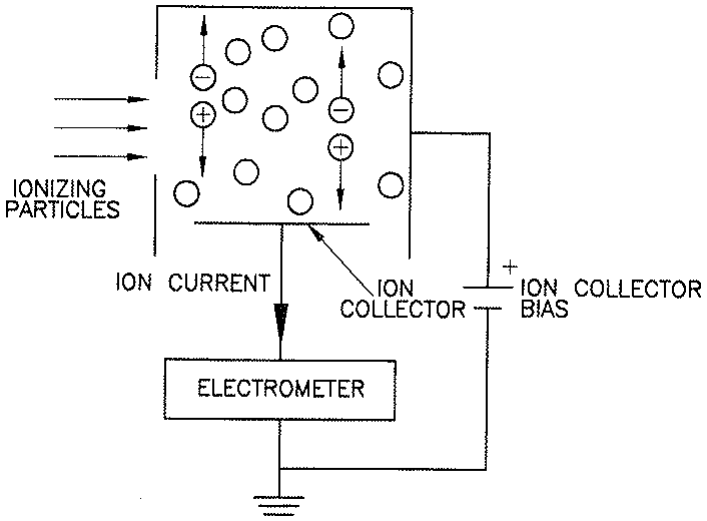

Figure 3.7: Generalized lay-out of an ionization gauge

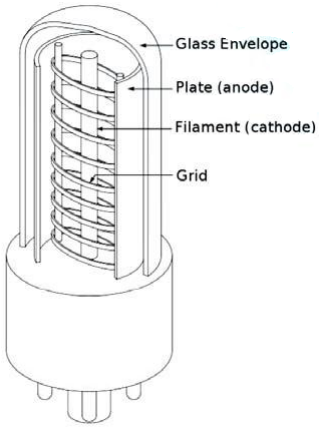

Figure 3.8: Bayard-Alpert ionization gauge

The number of ions formed is a function of the number of molecules per unit volume, the ionization cross section energy, arrival rate and electrons path length. The ionization gauge equation states the relationship between these quantities:

$$\imath_+ = \frac{\sigma_i L\ N\ q}{kT} \cdot p \tag{3.15}$$

where σ_i is the total ionization cross section for a gas molecule, L is the length of ionizing space, A is the cross-sectional area of the electron beam, N is the number

of electrons of charge q and p/kT is the number density of molecules. Therefore defining $K = \sigma_i L\ N\ q/kT$ as the gauge constant (or sensitivity) and $i_- = N\ q$ as the electron current equation (3.15) becomes:

$$i_+ = K i_- p \tag{3.16}$$

The sensitivity of the gauge can be improved increasing the path length L or designing the voltage in order to have the maximum ionization cross section σ_i (see Figure 3.9).

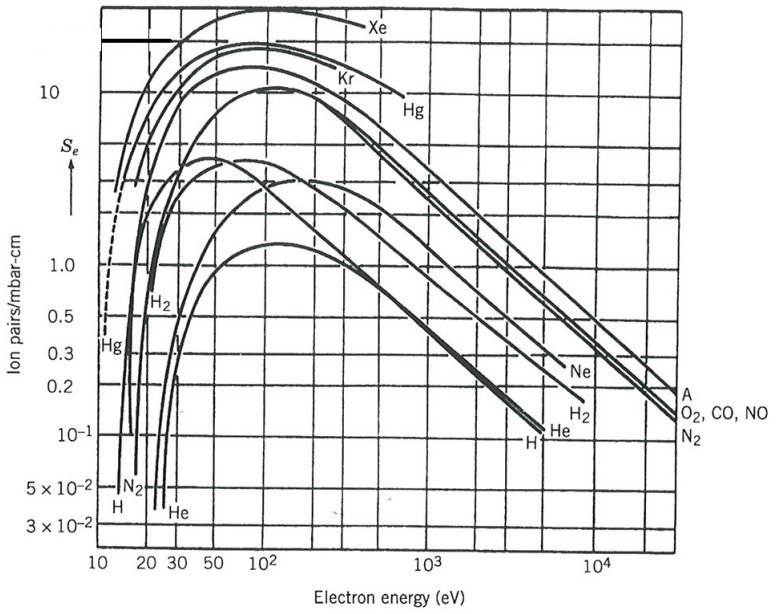

Figure 3.9: Ionization cross section dependence on electron energy

Actually the collector current is the sum of the ions current i_+ and a residual current i_r, which may have different contributions:

$$i_c = K i_- p + i_R \tag{3.17}$$

In the first hot-cathode gauge, i.e. triode configuration, the ion collector was a metal cylinder surrounding the grid and the cathode and the main contribution to the residual current was the so called x-ray effect. The electrons striking the grid produce soft x-rays which in turn cause photoelectrons emission from the surrounding ion collector.

The previous effect has been reduced by a factor of 1000 in the Bayard-Alpert configuration reducing the surface of the collector. The other components of the residual current are ESD induced on the grid and the so called "reverse x-rays effect"(Figure 3.10 shows both the x-rays involving effects). In the last case x-rays which strike the interior wall of the gauge can free electrons. Since both wall and collector can be grounded, some of these electrons can reach the collector causing a current of sign opposite to the normal x-ray current.

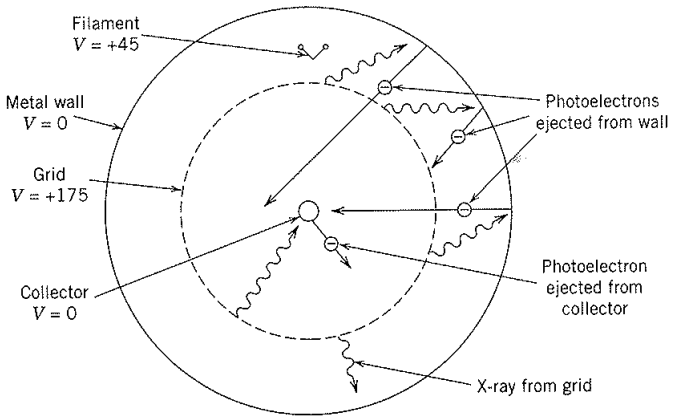

Figure 3.10: Section through a Bayard-Alpert Gauge illustrating the "normal" and "reverse" x-rays effect

Typically, a Bayard-Alpert gauge is accurate down to $1 \cdot 10^{-10}$ $mbar$. Further improvements of the B-A gauge have been development at CERN (Benvenuti and Hauer) by increasing the grid volume and the detection limit was lowered to $1.3 \cdot 10^{-12}$ $mbar$.

Cold-cathode gauge: Penning

The cold-cathode gauge is made of two electrodes: a cathode and an anode between which a high voltage is applied. Due to the high potential the cathode undergoes field emission and the emitted electrons are accelerated toward the anode. In their path they ionize the gas molecules, which ignites a self-sustaining gas discharge. To increase the electron path (electron trajectories are shown in

Figure 3.11) and therefore increase the ionization, and in turn the sensitivity of the gauge, a permanent magnet is placed on the exterior in order to generate an axial magnetic field in the Penning gauge .
The upper measurement limit is due to the fact that at pressure higher than 10^{-3} $mbar$ the mean free path is so long than the neutralization of the ions species occurs before the cathode could collect them. The lower pressure measurable is about 10^{-9} $mbar$: at lower pressure the charge density is low and it is difficult to sustain the gas discharge.

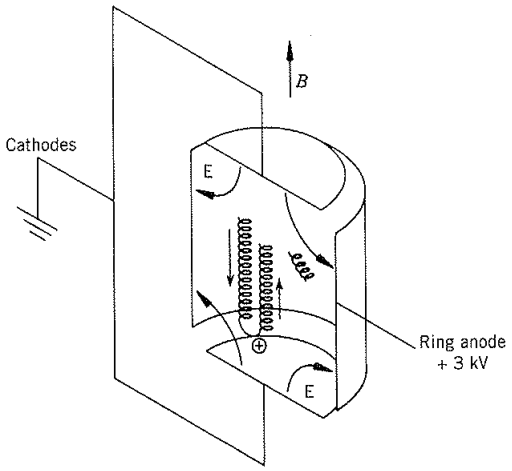

Figure 3.11: Penning gauge lay-out, electrons trajectories and magnetic field

3.2.1 Residual Gas Analyzer

The Residual Gas Analyzer (RGA) is one of the widely used mass spectrometers for partial pressure measurement in vacuum technology.
A ion source (usually electron emitted by a thermionic source filament) ionizes neutral gas particle, which are then sorted in the mass filter on the basis of their mass-to-charge ratio m/e. This separation is achieved by means of a quadrupole mass filter.
The quadrupole mass filter consists of four parallel rods arranged in a square array with opposite rods connected electrically in parallel. The ions enter the quadrupole near the z-axis (refer to Figure 3.12) with a kinetic energy of $3 \div 15$ eV. The combination of a direct current potential and radio-frequency potential accelerate the

ions perpendicular to the z-axis. Just the ions with a small range of m/e can oscillate with small amplitudes and drift through the quadrupole filter without collisions with the rods. Higher m/e ions do not gain a huge x-y displacement during the RF cycle, but they are accelerated by means of the dc potential toward the negatively biased rods. Once they strike the rod they are neutralized. Ions with lower mass-to-charge ratio, instead, move nearly in phase with the rf potential and are accelerated to large x and y displacements. Also these ions are neutralized by impact with rods.

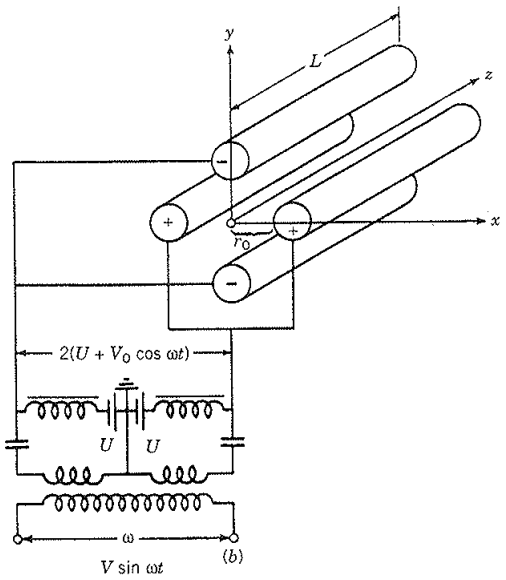

Figure 3.12: Quadrupole mass filter structures

By changing the amplitude of the rf potential is possible to scan over different m/e ions.

After the separating system the ion current can be measured in two different modes: the Faraday detector setup or the secondary electron multiplier (SEM) configuration.

In the former mode the ions strike a Faraday cup (or plate). The detection occurs when electron current flows to the plate to neutralize the charge of ions. The current is measured by an appropriate electrometer circuit and the current detection is limited to 10^{-15} A due to the noise. Moreover if smaller ion currents have to

be measured or if high measuring speed is required, the secondary electron multipliers (SEM) are used. The ion incident on the detector surface releases electrons which are converted into a larger signal with a multistage amplification of the electrons current. Usually the amplifier is made by cylindrical pieces of metal coated with high-Secondary-Electron-Yield material (dynodes) connected in series with a 100 V potential applied between each other. The amplification factor results in a huge increase ($10^4 \div 10^5$) of the sensitivity and of the signal-to-noise ratio. One of the disadvantages of SEM detection is that the number of electrons generated by a colliding ion effected the ion energy.
A data analysis system process the ion current value that is a parameter of the partial pressure of the respective gas molecules. A typical RGA spectrum (Ion current over mass) for a baked vacuum system is shown in Figure 3.13.

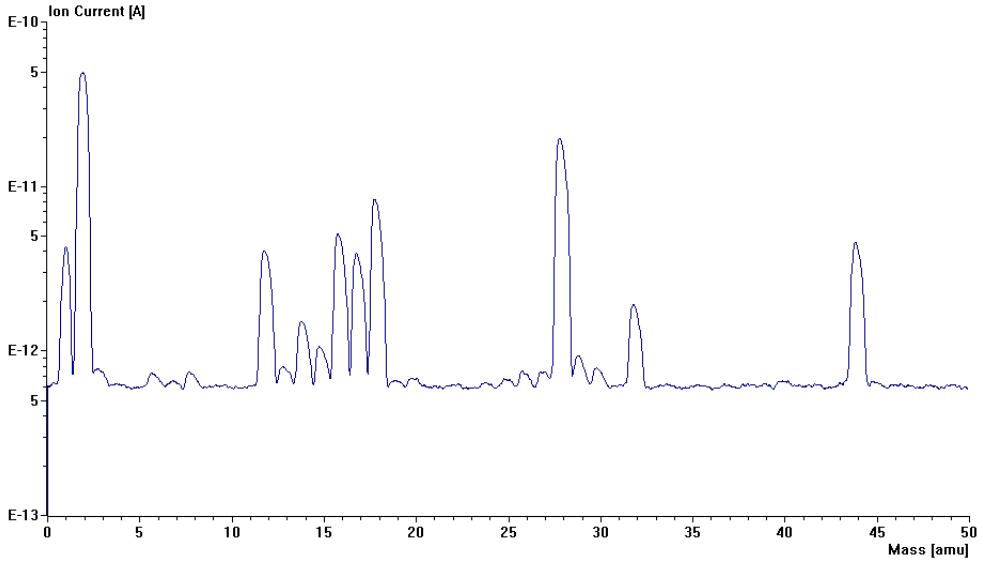

Figure 3.13: RGA spectrum: ion current versus mass

The same m/e value, and then the same peak, can be related to different gas species. For instance the mass 28 could be related to N_2 or to CO. To evaluate precisely the partial pressure of the two different species a calibration of the mass spectrometer is needed. In addition the concept of "cracking pattern" is useful to estimate the content of the specific gas specie in the gas mixture measured. The molecular species not only are ionized by the electrons from ions source but also

suffer cracking.
The example of nitrogen molecule it is shown hereafter.
This single ionization reaction leads to a peak at 28 u.m.a.:

$$N_2 + e^- \rightarrow N_2^+ \tag{3.18}$$

The ion, furthermore, can be ionized twice:

$$N_2^+ + e^- \rightarrow N_2^{++} \tag{3.19}$$

Otherwise the electron-molecule collision can lead to the following cracking:

$$N_2 + e^- \rightarrow N + N^+ \tag{3.20}$$

The last two reactions give a contribution at 14 u.m.a. .
To take into account this phenomenon, the relative ion current of fragment ions are usually listed for the most encountered gas species in vacuum application (see Table 3.1).

m/e	H_2	CH_4	H_20	Ne	N_2	CO	C_2H_6	Ar	CO_2
1	3	16.5	2.4				9.6		
2	100								
12		3				6.3	0.7		9.7
13		7.8					1.2		
14		16			14	0.8	3.3		
15		85					4.7		
16		100	1.8			2.8			16
17		1.2	26						
18			100						
20				100				22.6	
22				10.2					2.1
25							3.8		
26							22.2		
27							33.4		
28					100	100	100		13
29					0.7	1.2	20		
30							22.2		
36								0.34	
38								0.06	
40								100	
44									100

Table 3.1: Relative ion currents of fragment ions for 90 eV energy of ionization

3.3 Measurement Process: optimization

Experimental sequence

To calculate the desorption yield the partial pressure and the electronic current impinging on the sample have to be measured. This is done respectively by means of the RGA and the electrometer connected to the sample holder.
The RGA is controlled by the QuadStar32, a commercial software which allow to measure the ionic currents of several species, to tune the RGA and to display and convert the saved data in ASCII file (for later analysis). Firstly, once the sample is loading on the support, a spectrum is taken with the RGA in order to see which gas species there are inside the chamber and set RGA parameters to record the partial pressure over time. The power supply and the electrometer are controlled by a LabVIEW program designed expressly to run ESD measurement. This software allows the setting of the desired voltage on the sample holder and the reading/saving of the electronic current measured by both the electrometers. In this way it is possible to check if the two currents are the same during experiments.
The desorption measurements are done in pulse mode (the time duration of the biasing pulses is set by the LabVIEW program) in order to recover and verify the background pressure between one pulse and the other. Therefore the pressure measured by the full range gauge is monitored and the sample is biased again only when the background value is recovered.
The typical desorption pulsed signal recorded on the RGA is shown in Figure 3.14 (the numebr of cycles is proportional to the time). Several pulses have been recorded in order to measure the desorption yield over a wide range of electron dose.

It is essential to carefully control the value of the current flowing into the tungsten filament: higher value of the current lead to higher value of the desorption signal. Therefore it takes longer time to recover the background value and the sample warm up as the electron current rises. On the other hand if the surface is cleaned ("conditioning" after a certain dose, refer to 3.4) it is necessary to increase the current to have a detectable desorption signal.

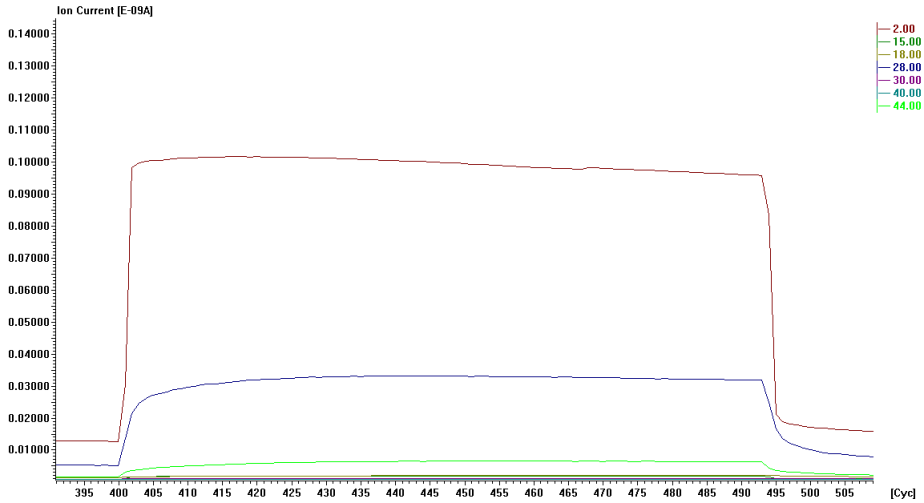

Figure 3.14: RGA signal for desorption pulses 300 seconds long.

3.3.1 Pumping speed calculation

It has been already stated in section 3.1 that, at a particular pressure p, the volumetric flow rate due to a pump is:

$$\dot{Q} = \frac{d(p \cdot V)}{dt} = p \cdot \frac{dV}{dt} = p \cdot S \tag{3.21}$$

where S is the pumping speed.

The pumping speed available at a real vacuum chamber will be affected by restriction due to connecting pipework. One of the most common problems in vacuum technology is to estimate the loss in speed due to such restrictions.

Knudsen introduced the notion of a pipe as an impedance in the electrical sense and Dushman introduce the concept of *conductance*, which is defined by the relation

$$C = \frac{\dot{Q}}{P_u - P_d} \tag{3.22}$$

where P_u is the upstream pressure and P_d is the downstream pressure.

Gas flow conductance is thus analogous to electrical conductance, with pressure difference being the analogue of voltage difference and $\dot{Q}$ the analogue of current. Applying the concept of reciprocal of impedance, the net conductance of a set of pipe in series is then

$$\frac{1}{C_n} = \sum_i \frac{1}{C_i} \tag{3.23}$$

The net speed of a pump in series with a component or pipe is found in a similar way:

$$\frac{1}{S_n} = \frac{1}{S} + \frac{1}{C_n} \tag{3.24}$$

In the molecular regime [1], the solution of gas transport problems can be reduced to finding the conductance of the elements involved since conductance is independent of pressure or flow condition. The derivation of conductance, by theoretical or analytical methods, assumes that molecules arrive at the entrance plane of a duct from a chaotic gas, so that the entrance plane effectively behaves as a diffuse emitter (i.e. the distribution of molecules emerging is spherical due to the absence of preferred directions). Clausing first introduced the concept of *transmission probability*, denoted by α. If N_2 arrive at the entrance of a duct then the number of these which reach the exit plane is $N_2\alpha$ and $N_2(1-\alpha)$ return to the entrance. Similarly, of N_1 molecules striking the exit plane, $N_1\alpha$ reach the entrance. The net flux of molecules from entrance to exit is then $(N_2 - N_1)\alpha$.

Expression for conductance are usefully formulated in terms of this transmission probability:

$$C_m = C_a\alpha \tag{3.25}$$

where C_a is the conductance of an aperture. The molecular flow conductance of a thin aperture with area A is defined as:

$$C_a = A\sqrt{\frac{R \cdot T}{2\pi M_m}} \tag{3.26}$$

where $R \approx 8.314\ J/(K \cdot mol)$ is the universal gas constant, T is the absolute temperature and M_m is the molar mass expressed in kg/mol. Therefore the unit of the conductance is m^3/s.

For instance, the expression for the transmission probability of a cylindrical tube of diameter d and length l is [17]

$$\alpha_c = \frac{4d}{3l} \tag{3.27}$$

In case of shorter ducts the previous formula is an overestimate, then the transmission probability relation is:

$$\alpha = \frac{\alpha_c}{1 + \alpha_c} \tag{3.28}$$

[1] If the mean free path of molecules is of the same order as, or greater, the characteristic dimension and gas dynamic are dominated by molecular collisions with the walls of the retaining vessel or pipe the regime is defined *molecular flow*.[17]

It is important to calculate the net pumping speed of each gas species recorded by means of the RGA during the measurement in order to estimate correctly the desorption yield (3.1). Considering the system geometry shown in Figure 3.15 one has to take into account the conductance of the calibrated orifice (C_a), the short duct between it and the lower chamber (C_d) the net pumping speed S_i is given by the formula:

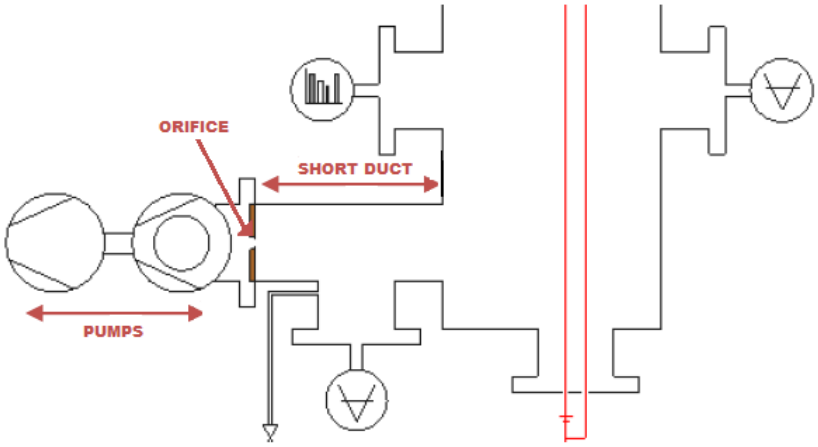

Figure 3.15: Lower vacuum chamber, highlight on the three elements introducing the vacuum impedance

$$\frac{1}{S_i} = \frac{1}{S} + \frac{1}{C_a} + \frac{1}{C_m} \tag{3.29}$$

where S_i is the pumping speed for each gas species which are pumped with a different pumping speed (e.g. for hydrogen $S_{H_2} = 46\ l/s$). Therefore the values for the net pumping speed are: For the calculation of the net pumping speed (refer to equation (3.29)) the values listed in the third column of Table 3.2 become negligible by a comparison with the values of the aperture conductance. The role of the orifice (3.6 mm diameter) is just to reduce the pumping speed in order to make the desorption signal detectable by the RGA. If the desorbed gases are pumped away quickly no signal would be recorded.

Gas	C_a $[m^3/s]$ x 10^{-3}	C_m $[m^3/s]$ x 10^{-1}
H_2	4.535	4.954
CO/N_2	1.212	1.324
H_2O	0.967	1.651
CH_4	1.603	1.751
C_2H_6	1.171	1.279
CO_2	1.512	1.056

Table 3.2: Conductance of the orifice and of the short tube for different gases species

Gas	S_i $[l/s]$
H_2	4.128
CO/N_2	1.183
H_2O	1.467
CH_4	1.553
C_2H_6	1.144
CO_2	0.948

Table 3.3: Conductance of the orifice and of the short tube for different gases species

3.3.2 Pumpdown and duration of desorption peak

The pumping speed influences the desorption yield measurement also in term of duration of desorption peak.
Calculating the time-dependence of the pressure in the system can be useful to understand this statement. Starting from a flux balance, and with the assumption of constant gas temperature, it is possible to write the following differential equation:

$$V \cdot \frac{dp}{dt} = \dot{Q}_{in} - \dot{Q}_{out} \tag{3.30}$$

where $\dot{Q}_{in}$ is the desorption source and $\dot{Q}_{out}$ is the flow the pump system removes from the chamber:

$$\dot{Q}_{out} = p \cdot S_n \tag{3.31}$$

In a real system the pumping speed is strongly pressure-dependent and the flow is generally a function of time and can be pressure-dependent as well. The simplest assumptions are pressure and time independent constant pumping system and flow. Therefore, the pressure in the system has this time-dependence:

$$p(t) = \left(p_0 - \frac{\dot{Q}_{in}}{S_n} \right) exp\left(-\frac{S_n}{V} t \right) + \frac{\dot{Q}_{in}}{S_n} \tag{3.32}$$

where $p_0 = p(t = 0)$ is the initial condition and $\dot{Q}_{in}$ is the desorption rate. This function is plotted on the left side of Figure 3.17. Defining the time constant as $\tau = V/S_n$, one can see that if the pumping speed is too slow it will take more time reach the plateau. It is possible to control the peak duration controlling the high voltage which bias the sample holder. This time should be set in order to make all the gas species reaching the plateau value. The previous measurements were taken for pulses 20 s long. While the new copper sample was tested, the duration was increased to 300 seconds (the typical shape for 20 seconds long pulse in Figure 3.16 for a visual comparison with the 300 seconds long pulse shown in Figure **??**).

The sample sits on a support which has a same-shaped hole to fit it (refer to Figure 3.1). However there is a small space between the sample and the sample support through which the gas desorbed in the small volume between the sample and the butterfly valve can flow. The pumping speed calculated in the last section

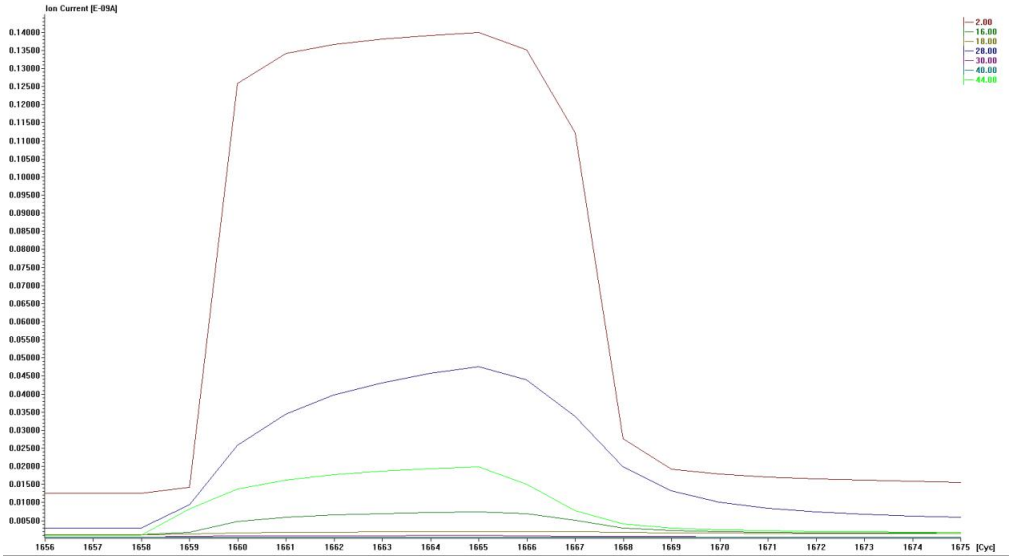

Figure 3.16: RGA signal for desorption pulses 20 seconds long

is actually influenced also by the time needed to fill this volume.
The real time-dependence of the pressure in the lower chamber p_1 is given by the following differential equation system, where the index 2 is referred to the upper chamber:

$$\frac{dp_1}{dt} = -\frac{p_1 \cdot S_1}{V_1} + \frac{\dot{Q}_1}{V_1} - \frac{S_1(p_1 - p_2)}{V_1} \tag{3.33}$$

$$\frac{dp_2}{dt} = -\frac{S_2(p_2 - p_1)}{V_2} + \frac{\dot{Q}_2}{V_2} \tag{3.34}$$

In Figure 3.17, on the right side, $p_1(t)$ is plotted in blue (numerical solution of the system of equation) while the red function is the plot of (3.32)). It has to be noted that the time needed to fill the upper chamber influences the time-dependence of the pressure in the lower chamber. The recorded pressure (the RGA is connected to the lower chamber) reaches the steady state condition in a longer time.
The space between the sample and the support can be estimated as an annulus [17] $\sim 10^2\ \mu m$ wide. The pumping speed of the upper chamber S_2 has to be calculated considering this annulus conductance which, due to the dimension, is not negligible compared to the orifice conductance. In particular, the time constant $\tau_1 = V_1/S_1$ of the lower chamber and the time constant of the second volume τ_2 are shown in

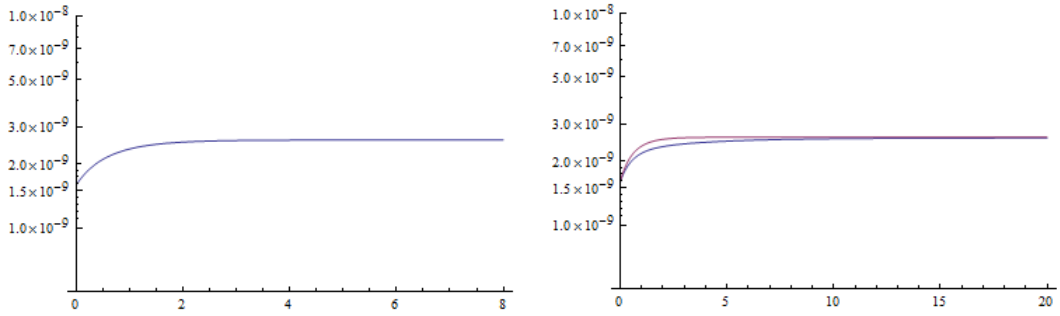

Figure 3.17: On the left, blue line: Pressure rising in a chamber during desorption. On the right: comparison of it (red line) with the same pressure but influenced by the presence of a second volume to be filled (blue line).[Time scale is different].

the third column of Table 3.4.

Gas	τ_1 $[s]$	τ_2 $[s]$
H_2	0.70	47.9
CO/N_2	2.45	179
H_2O	1.97	143
CH_4	1.86	135
C_2H_6	2.53	185
CO_2	3.05	224

Table 3.4: Pumping time constant for lower chamber (τ_1) and for the volume between the sample support and the butterfly valve(τ_2)

Improvement of the system

If the desorption pulse lasts $\sim$ 20 s most of the gases do not reach the plateau (see Figure 3.16). The reason is that the rising time of the pressure in the lower chamber is influenced by the gas which fills the small volume above and afterwards passes through the "annulus conductance". Therefore the pressure takes more time to reach the steady state condition and obviously also to be pumped down (the behaviour is symmetrical).
To avoid this problem for the next measurements, an hole of $\sim$ 5 mm has been

drilled in the sample support. In this way an aperture conductance has been introduced, but due to its dimension this conductance becomes negligible in the calculation of pumping speed.
In other words there is no more a high resistance to the flow of gas and the desorbed molecules diffuse quickly in the lower chamber. The following measurement will be done with shorter desorption pulse in order to have more data in the same range of dose than the case of measurement with 300 *seconds* pulse long.

3.4 Data

The second sample tested, belonging to the official sample campaign, is the 54-SSH104C. This sample has been cleaned with a chemical etching according to SLAC (National accelerator center in Standford, California) mixture(first S); it has been produced at SLAC (second S) and thermal treated under an hydrogen pressure of 1 bar (H) at 1040° C (104).
The desorption yield data for bombardment of this sample with electrons at 10 kV are shown in Figure 3.18. Each dot represent an average value relative of a desorption pulse (considering the pressure value in the plateau zone).
The ranking of the gaseous signal is expected with N_2/CO and H_2 having the highest signal.
The effect of the electron dose is to decrease the electron induced desorption yield. This phenomenon is known under the generic term of "conditioning".
In Figure 3.19 data related to desorption yield at 10 keV electrons for 19-PCV082C are shown. This is the first tested sample of the sample campaign. It has been cleaned with passivation surface treatment (P); it has been produced at CERN (C) and thermal treated under vacuum (V) at 820° C. Both samples have been tested with the same set-up and the same electron energy.
It has to be noted that the desorption yield values in Figure 3.18 are lower than the values in Figure 3.19 by a factor 5. On would expect a bigger hydrogen desorption yield from the sample 54-SSH104C and actually it do not. One hypothesis is that the time passed between the treatment and the measurement as well as the storage condition (package condition, time spent at air) influence the behaviour of the samples much more than heat and surface treatments.

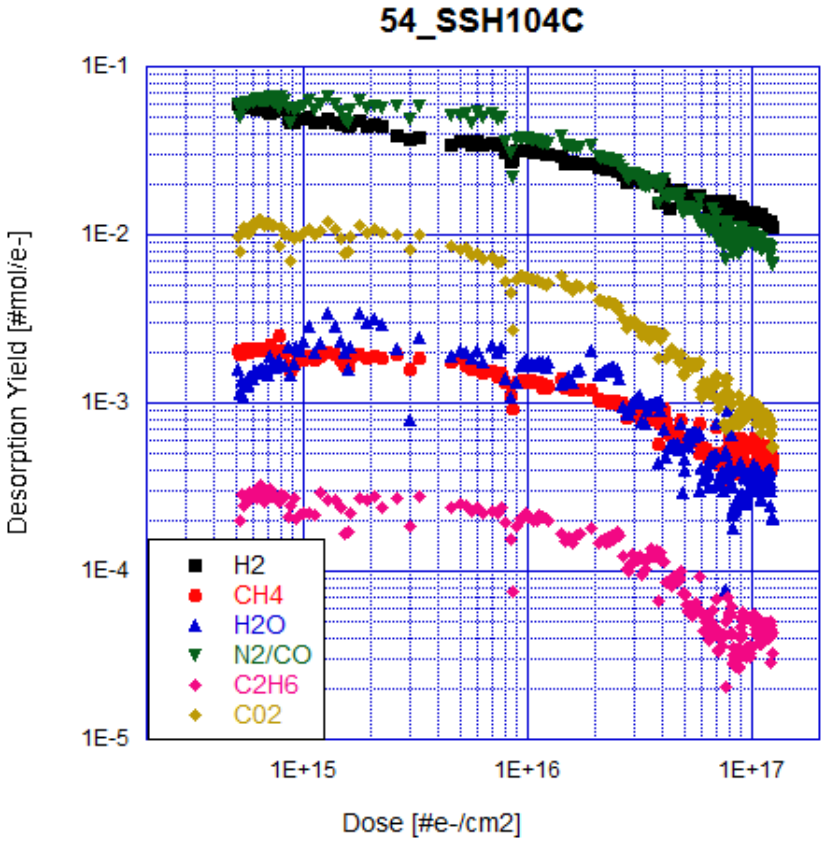

Figure 3.18: Desorption Yield experimental data for 54-SSH104C at 10 kV electron energy

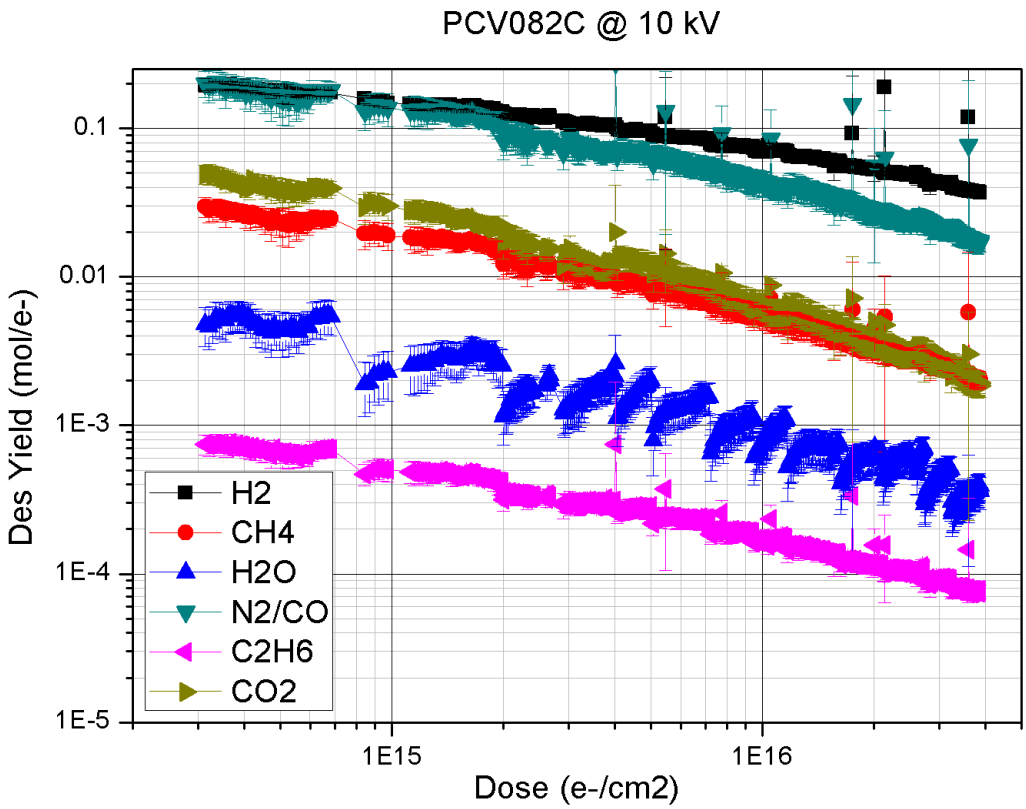

Figure 3.19: Desorption Yield experimental data for 19-V082C at 10 kV electron energy

Electron Energy correlation

Some desorption yield measurements were done for different voltage applied at the sample holder in order to investigate the electrons energy correlation. The data shown in Figure 3.21 are related to very first experiments on 54-SSH104C while in Figure 3.22 are plotted the data related to the same sample but after having tested it at 10 kV up to a dose of $1.2 \cdot 10^{17}$.
When charged particles interact with matter they lose their energy due to ionization and excitation of the atoms of the material. Lose of energy by radiative process is as well significant for quite energetic electrons. To describe this phenomena one usually refer to *Stopping power* $S = -dE/dx$ $[MeV/cm]$, i.e. the differential energy loss for the particle within that material divided by the corresponding differential path length[19]. The stopping power is described by the Bethe-Bloch formula and its corrections (for details refer to [19]). Often to compare different materials it is possible to use the stopping power divided by the absorber medium density, which units are $[MeV\ cm^2/(g)]$.
In Figure 3.20 the stopping power for electrons in copper is plotted for the energy range of interest. There is a clear decreasing trend for the stopping power

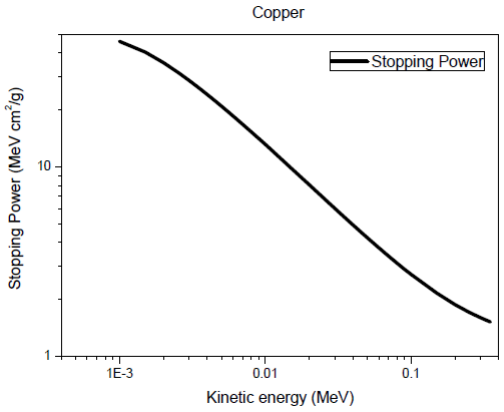

Figure 3.20: Stopping power $[MeV\ cm^2/g]$ for electrons in copper

as the electrons energy increase. The electrons lose less energy per unit path at high energy, therefore the desorption yield is supposed to decrease as well. This expectation is confirmed by the experimental data: the desorption yield, after an initial increase at low electron energy, slightly decrease for energy above 10 keV.

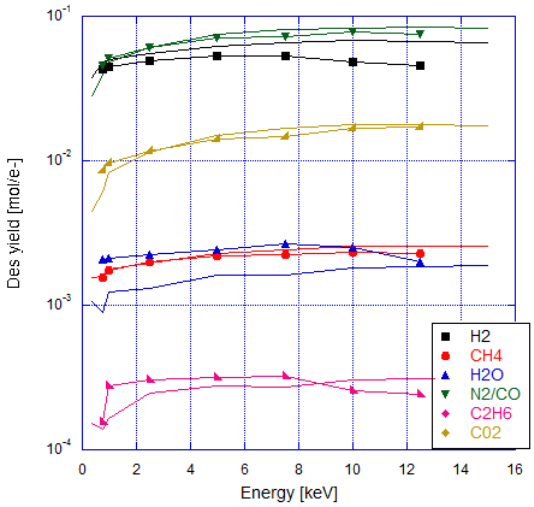

Figure 3.21: Desorption Yield over electron energy

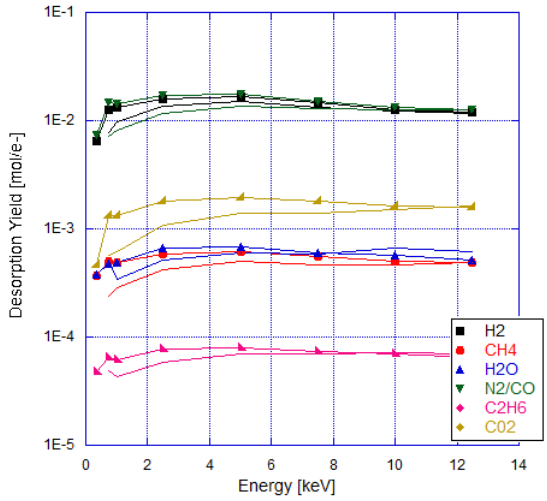

Figure 3.22: Desorption Yield over electron energy after tested it up to a dose of $1.2 \cdot 10^{17}\ e^{-}/cm2$

3.5 Discussion and Outlook

The sensitivity of the measurement of desorption yield is mostly related to the background pressure of the system: the lower this pressure is the lower is the limit of detection.
Contribution to this background pressure for the experimental set-up used are outgassing of the heated filament (the electron source, the filament of the RGA and of the B-A gauge)and leaks. Therefore the B-A gauge is switched off during the measurement and the current flowing in the source filament is kept low to reduce the contribution.
Moreover the sample is bombarded for a small amount of time (5 minutes) so that in between one measurement and the other the system recover the initial value of the background pressure preserving the limit of detection.

The experimental errors related to each spot in desorption yield versus dose plot have been calculate taking into account the standard deviations of the pressure in the desorption plateau σ_{p^1}, the standard deviation of the background pressure σ_{p^0} and the standard deviation related to the current impinging on the sample σ_I.
The desorption yield error is given by:

$$\sigma_\eta = \sqrt{\left(\frac{\delta\eta}{\delta\Delta p}\cdot\sigma_{\Delta p}\right)^2 + \left(\frac{\delta\eta}{\delta I}\cdot\sigma_I\right)^2} \tag{3.35}$$

Therefore, from the definition of the desorption yield η ((3.10)), the error is:

$$\sigma_\eta = \sqrt{\eta^2\left(\frac{\sigma_{p^1}^2 + \sigma_{p^0}^2}{(p^1 - p^0)}\right) + \frac{\sigma_I^2}{I^2}} \tag{3.36}$$

The experimental data with error bars are are shown in Figure 3.23. The errors are symmetrically extended above and under the average values. It has to be noted that all the sources of error have been taken into account and that there are some outliers meaning that some accidents happened during the desorption measurement. The side of the sample holder was filed leaving a higher roughness on the surface, probably creating field emitters. This field emitters can in turn trigger a spark and therefore an extra electron source. The sample holder will be further modified to suppress this problem.

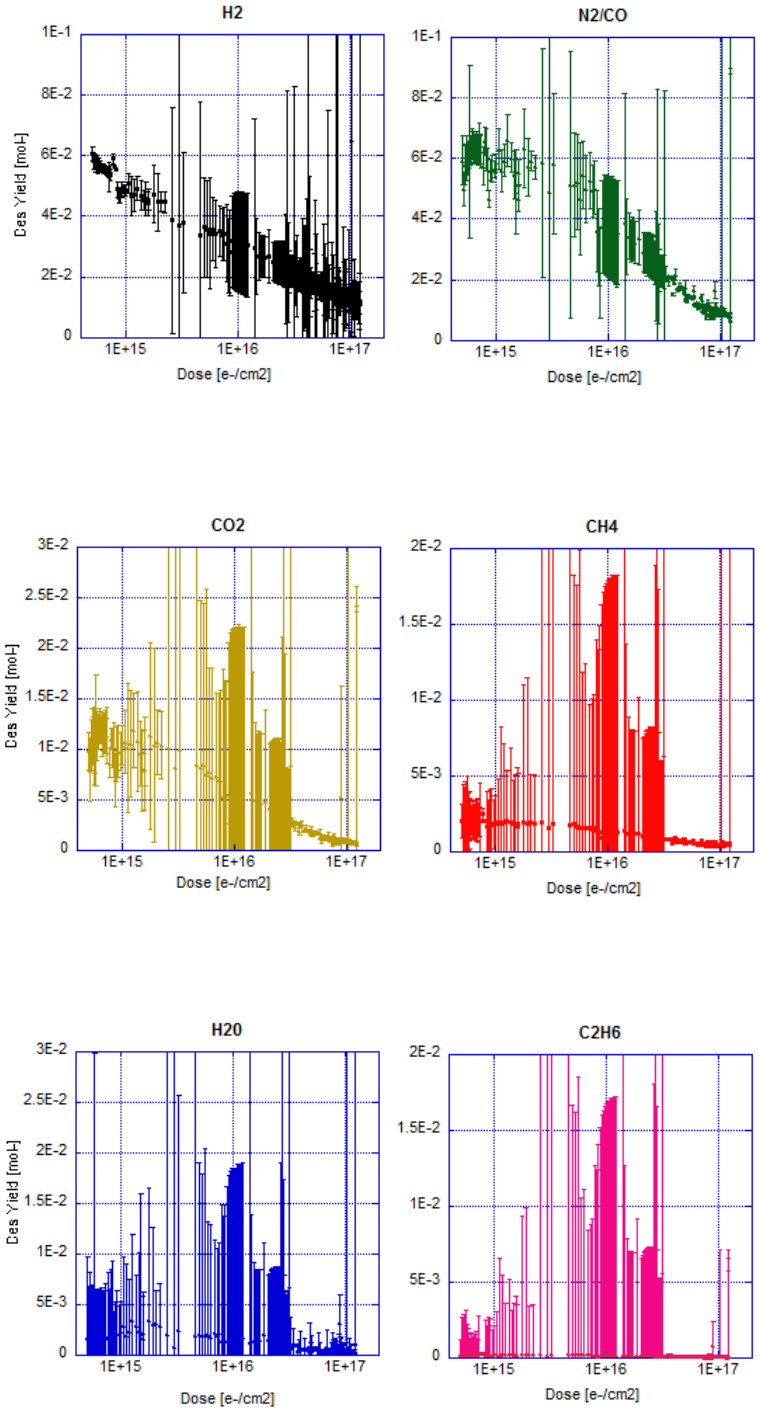

Figure 3.23: Desorption Yield data with error bars for each gas species

The desorption pulse duration has been increased during the test of the sample 54-SSH104C to let all the gases reach the plateau value in order to have more reliable data. Considering the improvement implemented on the system in the future one will be able to do the measurement with shorter pulses. In this way it will be possible to preserve even more the detection limit related to the background pressure. Moreover the heating of the sample will be much reduced and more desorption yield data points could be recorded in the same range of electron dose. In the future the whole testing campaign will be developed leading to a final choice of treatment of copper. The next suggested step is to test the twin samples (same cleaning and same thermal treatment) of the samples already tested to check the reliability of the measurement.

Chapter 4

Development of Laser Ablation for Hydrogen Content measurement in metals

Laser beam induced processes in materials have been studied and applied as attractive tools and research instruments in many different areas of material science. The encouraging results of gas amount measurement in thin-films by laser ablation performed here in the past years [23] have given the motivation to this work. In these experiments on thin-films produced by sputtering it was possible to estimate the argon content with an uncertainty of $\pm 12\%$ (in addition to $\pm 20\%$ of systematic error for the calibration of the gas analyser) for 1 to $2\mu m$ thick films of different materials (Ti ,V, Nb, Mo,..) deposited both on glass and on copper substrates.
The aim of this work was to make the necessary improvements and changes in the measurement process to investigate the possibility of hydrogen content measurement in metals, especially OFE copper.
It has to be noted that this kind of experiment has never been done before to our knowledge and that we were aware of the difficulties we would encounter during this experimental activity.

4.1 Experimental Setup

The experimental setup can be divided in to two main parts: the vacuum system and the optical system.

4.1.1 Vacuum system

As shown in Figure 4.1 the vacuum system is composed of two different vacuum chambers: Ablation Chamber (AB) and Analyses Chamber (AC) communicating together by several by-passes and valves.
Each vacuum chamber is connected to a pumping system made up of one primary pump and one turbomolecular pump (TMP). At the top of each pumping system there is a dual gauge and two pneumatically operated valves. The dual gauge is made up of two separate measurement systems (Pirani system and cold cathode system) which behave as one uniform measurement system. Others vacuum gauges are connected to the system: one capacitance gauge on the top of the AB chamber and one Bayard-Alpert gauge connected to the AN chamber via a small conductance.
On the top of the AN chamber there is the residual gas analyzer (RGA), i.e. de mass spectrometer (more details on vacuum gauges and RGA can be found in Chapter 3). The gas bottle is connected directly both to the top and the bottom of the AN chamber, but also to the top of the pumping line of the same chamber. From AB chamber the main by-pass goes to the AN chamber passing through the cold trap (the walls of this part of line are cooled by immersion in liquid nitrogen). The other is linked to the gas bottle and to the other by-passes.
The reason of this layout is that the change in partial pressure versus time are recorded by the RGA which is connected to the AN chamber. Therefore, while the measurement is done, the AB chamber, inside which the targets are placed, is under static vacuum and the gas is pumping by the AN pumping group.
The most used by-pass is the one that pass through the cold trap that is useful to trap most of the gases desorbed from the ablation chamber except hydrogen. To understand the importance of the cold trap note that the sensitivity of the RGA is strongly dependent on the composition of the gas mixture and that in the early experiments the AB was filled through the injection line with the "buffer gas" until

a pressure of $1 \cdot 10^{-2} mbar$(more details in 4.2).
The samples are loaded and set in the right position using a rotary feedthrough and a plate on the top of it. It this way it is possible to load different samples into the system and testing them one at a time.

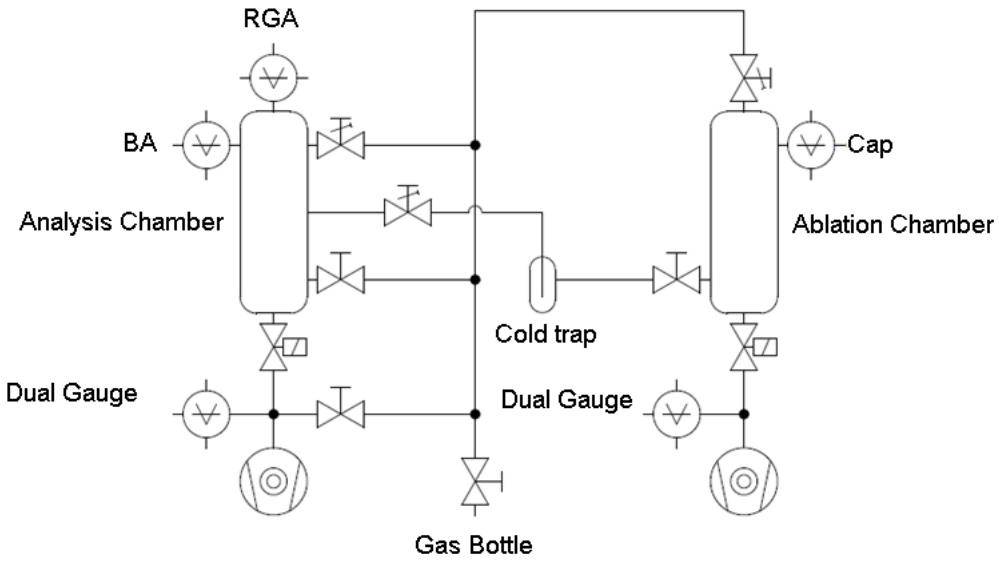

Figure 4.1: Vacuum System Layout

4.1.2 Optical System

Figure 4.3 shows the schematic layout of the laser beam delivery optics system. The beam produced by an Excimer Laser (see Table 4.1 for specifications) pass through mirrors to be bent. An homogenizer and a mask (slit dimensions $10X10\ mm^2$) coupled with a lens have been introduced in the optical line to homogenize the intensity and reshape the profile of the output beam . The attenuator and the Joulemeter have been used to control the energy transmitted and measure the energy of the pulses respectively.
The optical elements (summarized in Table 4.2) are described in detail hereafter.

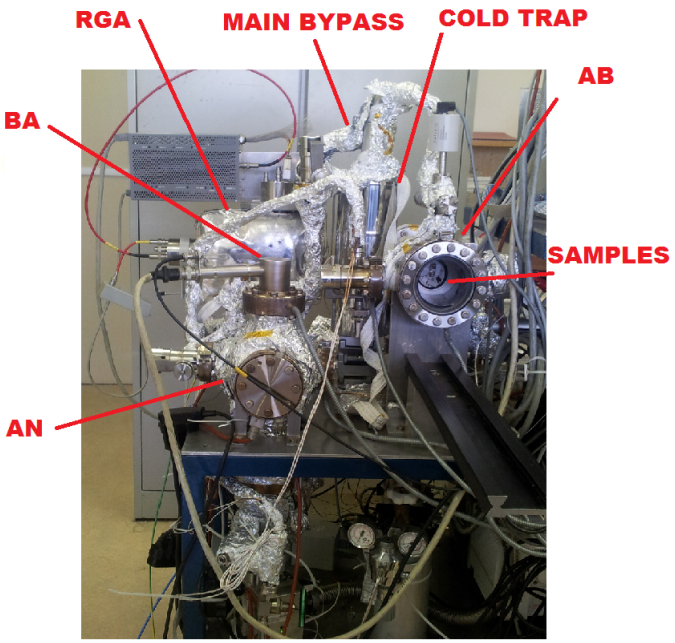

Figure 4.2: Pictures of the vacuum system used for ablation experiment

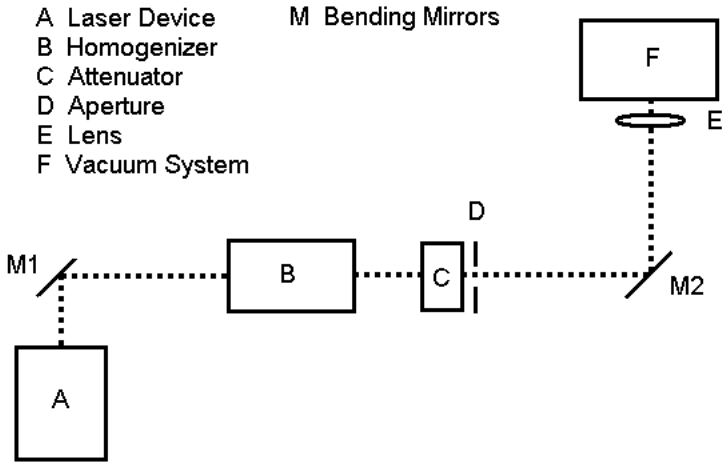

Figure 4.3: Delivery Optics System

Laser type	Compex Pro 110 F
Test gas	KrF ($\lambda = 248\ nm$)
Average pulse energy	300 mJ
Pulse width	20 ns

Table 4.1: Excimer Laser specification

Homogenizer	COHERENT 11/2006
Attenuator	AT4040 Energy Controller
Joulemeter	Molectron JD 1000
Lens	Focal lenght: 217mm at 546nm

Table 4.2: Optical elements

Homogenizer

The homogenizer consists of 2 crossed arrays (for a dual axis homogenizer) of cylindrical lenslets and a condenser lens mounted to special optics mount to align in all directions without unscrewing the optical elements. An n-element array of cylindrical lenslets serves to divide the input beam profile into n slices. Each of these input slices is then expanded and mapped across the entire output beam profile, which is accomplished by a second lenslet array and a single reimaging lens. The output profile thus consists of the average of the profile of the individual slices. Figure 4.4 shows the operation principle for a single axis homogenizer (for the other beam axis a similar array setup is used): each beam segment of a given width d is projected to the full width D of the illumination field, which is located at the distance f_3 behind the curved surface of the condenser lens. All lens of the homogenizer are plano-convex with a specific focal length f, which is given through the equation:

$$f = \frac{r}{n-1} \tag{4.1}$$

where r is the radius of curvature and n is the index of refraction given for the specific laser wavelength. The homogenizer produces a beam with a very flat intensity profile in both cross section with an efficiency of 80%.

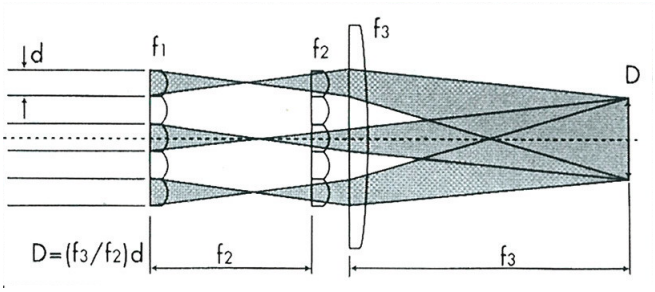

Figure 4.4: Operation principle of the homogenizer

Attenuator

For high power excimer lasers internal control over energy from within the laser source generally has an unwanted side-effect on the beam profile. Therefore a laser beam attenuator is needed to operate at different fluence.
The fundamental principle of this energy controller is the dependence of the cut-off wavelength on the tilt angle between the beam and a multilayer dielectric filter. Figure 4.5 shows the operation principle: the part of the beam which is not trans-

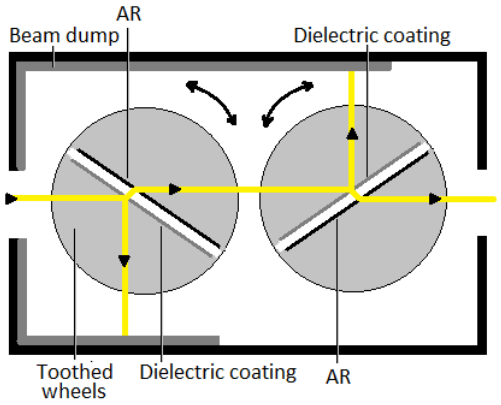

Figure 4.5: Attenuator layout

mitted is reflected, at twice the tilt angle or 90% for minimum transmission. This reflected component is scattered/absorbed in a light trap/heat sink surrounding the optics. Attenuator plates are specific to a particular wavelength and consist of fused silica plates with dielectric coating on the "attenuator side" and anti-reflection (AR) coating on the other side. The internal dc servo motor is used like

a stepping motor and is controlled by a specific software.
The coating is made so that the highest transmission, approximatively 95%, occurs with the attenuator plate perpendicular to the beam. Transmittance is reduced progressively with the tilt angle in a non-linear fashion (Figure 4.6) to low value typically $< 5\%$ at 45°. The open gate configuration removes optics completely from the beam leading to 100% transmission.

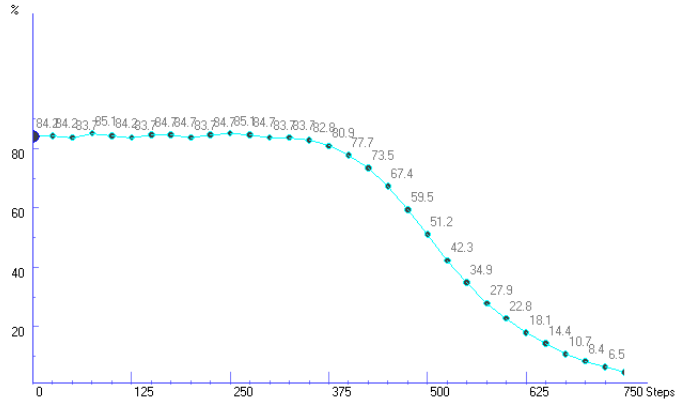

Figure 4.6: Attenuator transmission [%] over steps

Pyroelectric Joulemeter

The Pyroelectric Joulemeter belongs to the category of thermal radiation sensors, in which absorbed radiation is first converted to heat, which subsequently produces a measurable effect. The underlying principle of pyroelectric detection is the temperature dependence of the electric polarization in certain classes of materials, including most prominently ferroelectrics. In these solids the crystal lattice contains bound ions that are nonsymmetrically positioned, resulting in a spontaneous electric polarization. When a temperature change occurs, the lattice rearranges itself and shifts the ion positions, generating a polarization current until the temperature stops changing. Electrodes are applied on the surface of a "pole" pyroelectric solid (where the microscopic domains, usually randomly oriented, have been align parallel to a preferred polar axis). A temperature dependent polarization charge develops on these surface and a current is generated in an external circuit to neutralize the polarization charge. The pyroelectric joulemeter, due to

the cited features, ignore steady background radiation and has in general a wide uniform spectral response, good sensitivity and high speed.

Beam alignment

To perform the measurement the laser beam must be focalized on the sample to be tested. The converging lens used for this purpose has a focal length of $f = 217\ mm$ for $\lambda = 546\ nm$, it should be correct considering the laser wavelength $\lambda = 248\ nm$:

$$f_{(\lambda=248)} = \frac{n_{(\lambda=546)} - 1}{n_{(\lambda=248)} - 1} \times f_{(\lambda=546)} = 0.196\ m \tag{4.2}$$

where has been used the index of refraction of quarz: $n_{546} = 1.46\ mm$, $n_{248} = 1.508$. The relationship between the lens-object distance u and the lens-image distance v (in this case the object is a square slit of $A = a \times b = 1\ cm^2$ area and the image is on the sample surface)is described by the thin lens equation:

$$\frac{1}{u} + \frac{1}{v} = \frac{1}{f} \tag{4.3}$$

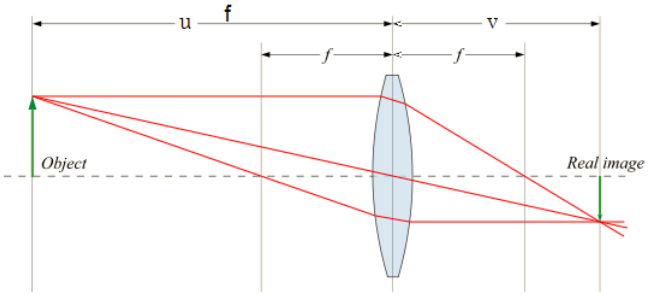

Figure 4.7: Thin lens equation scheme (converging lens, object-to-lens distance greater than focal length)

Once the energy E of the pulse is measured after lens by means of the joulemeter, the alignment parameters are set in order to obtain the desired fluence Φ. For measured energy of $E = 100\ mJ$ and to get $\Phi = 5\ J/cm^2$ the demagnification factor $D = u/v$, must be equal to:

$$D = \sqrt{\frac{\Phi A}{E}} = 7.017 \tag{4.4}$$

From (4.7) and the definition of demagnification:

$$u = (1 + D) \times f_{(\lambda=248)} \tag{4.5}$$

$$v = \frac{(1 + D) \times f_{(\lambda=248)}}{D} \tag{4.6}$$

therefore $u = 1.586\ m$ and $v = 0.224\ m$, whereas the dimension of the spot are $a/D = 1.4141\ mm$ ans $b/D = 1.414\ mm$. Putting thermal paper at a distance v from the lens it is possible to imprint a burn pattern on it and check the shape and the size of the spot.

Ablated Volume

The interaction of a high intensity pulse with a solid sample results in the crater formation. It is possible to use a white light interferometer to draw the profile of the samples after ablation.
Figure 4.8 gives the typical crater profile, obtained after 100 laser pulses at 2.5 W/cm^2 on Silicon. The crater profile did not correspond to the spatial laser intensity distribution, probably due to the recondensation process. On the target surface around the crater one can observe the presence of matter. The height of this matter around the crater depends on the target, the energy and the pulse number. These "bumps" are probably due to both re-deposition of evaporated atoms and locally melted material pushed away by plasma pressure. Global melting does not take place because the laser pulse is too short (20 ns). By means of the same interferometer is possible to estimate the volume in between the reference surface (grey line in Figure 4.8) and the profile surface of the crater , but even the volume in between the reference surface and the profile of "bumps". It has emerged that, for silicon samples, the second could be bigger than the former. The reason is that the re-deposited material is porous. Therefore the volume between the profile of the crater and the reference surface is taken as an estimate of material removed and henceforth one will refer to it as *ablated volume*.

4.2 Measurement Process

Even if the target material of this experiment is copper, to get start with the system and the ablation process, test on other kind of materials (Silicon and Silicon coated

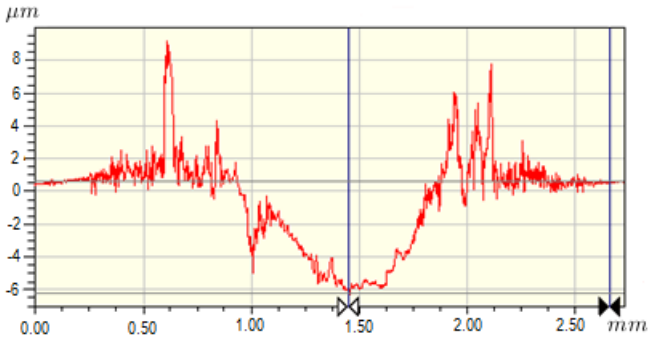

Figure 4.8: Typical central crater profiles for Si after 100 laser pulses

with a thin film of amorphous Carbon) have been performed. The reasons for this particular choice, however, are more solid. First of all it has been possible to take advantages from the previously reached experience with ablation of thin film. Silicon sample has been useful to estimate the "background", as the expected hydrogen content in it is negligible. Moreover it is easier to ablate silicon and coated silicon leading to better shaped crater and therefore an easier estimate of the ablated volume.

Hydrogen Content Measurement: experimental sequence

Referring to Figure 4.1 the experimental sequence for hydrogen content measurement is listed hereafter.

1. The Bayard-Alpert gauge and the dual gauge must be switched off. It was shown that these gauges, mostly the former, influence the pressure measurement. The pressure takes some time to stabilize, so the "recipe" is to switch-off the Bayard-Alpert at least 90 minutes before starting the ablation.

2. In order to have the same conductance and therefore the same pumping speed, the valve between the AB chamber and the cold trap is fully opened hence the leak valve between cold trap and AN chamber is opened always unscrewing the same number of turns (usually 6 turns and a half).

3. Once the cold trap is immersed in a container filled by liquid nitrogen, few

minutes are needed to cool down the trap.

4. The in-house software (LabVIEW) which runs the RGA is started to record the partial pressures during time. The gas species usually monitored are H_2, N_2, CO, CH_4, H_2O, but they are chosen after taking a spectrum of the mixture inside the chamber.

5. The pneumatic operated valve between TMP and AB chamber is closed in order to leave the AB chamber in static vacuum condition. At least 15 minutes are waited to let the hydrogen pressure stabilized to the background value due to the outgassing (see the next section).

6. The laser parameters (frequency, number of pulses and fluence) are set and the sample are shot with the beam.

The behaviour expected is then hydrogen partial pressure increase for a while and afterwards the recovery of a plateau from which the total quantity of hydrogen released (Q_{H_2})should be calculated. Measuring the ablated volume then, should be possible estimate the relative hydrogen content in the sample and compared it with theoretical calculations in order to get the sensibility of the measurement process.
Preliminary measurement on Carbon film on a Silicon substrate has been done following the steps listed in the previous paragraph. The released quantity of hydrogen measured was high, the ablated volume was easily measured and an average content of 1.5 Hat/Cat was estimated. The expected hydrogen quantity in carbon film is huge and not so far from this value. Therefore the first results were encouraging.
The expected hydrogen in copper sample, instead, is very low (see section 2.3). Therefore to get started, the system/process limits have been investigated.

4.2.1 System limit: Outgassing

It is well known that the chamber walls and the components within the chamber release gas which was adsorbed at the surfaces or entrapped in the volume of the material. Since it is not possible to predict the outgassing (spontaneous evolution of gas from solid and liquid) and degassing (the release of absorbed chemical

species from the surface) behaviour, measurements have been performed for the experimental system.
Henceforth the outgassing will include both bulk and surface phenomena.
The procedure followed is explained hereafter. Starting from Ultra High Vacuum (UHV) condition (i.e: pressure below $5 \cdot 10^{-9} mbar$ for both chambers), the partial pressures of hydrogen is recorded with the RGA. Leaving the BA gauge on and the gas flowing through the injection line (with cold trap not cooled), after few minutes ($t = 800s$ in Figure 4.9) the valve between the AB chamber and the pumping system was closed.
The pressure has been recorded for almost one hour but one can see that the steady state condition (i.e. the flat trend in Figure 4.9 is reached after 15 minutes.
At $t = 3800s$ the valve between AB chamber and TMP is re-opened to pump down the system.
The difference between the plateau value and the pressure at the beginning (which is equal to the pressure at the end) give the background pressure of the system.
Since the goal of this experimental setup is the measure of hydrogen content in metal and as that gas gives the major contribution at the outgassing, the attention is focusing on it. Taking into account the nominal pumping speed of the pump groups connected to the analyses chamber $S = 42\ l/s$ and calculated the pressure difference between the plateau value and the background when both the chamber are pumped ($\Delta p \approx 2.8\ mbar$), it has been estimated an hydrogen outgassing rate for the ablation chamber:

$$\dot{Q}_{H_2} = \Delta p \cdot S = 1.2 \cdot 10^{-8} \frac{mbar \cdot l}{s} \tag{4.7}$$

Therefore in the system there is an intrinsic limitation to be considered: assuming an average duration of the ablation peak of 1000 seconds (time needed after ablation on copper to recover the background 4.2.3), the minimum measurable quantity is in the order of $10^{-5}/10^{-4} mbar * l$.
This is a huge amount and an actual limitation for materials that even treated have a small concentration of hydrogen.

4.2.2 Process limit: dynamic hydrogen background

Another important issue is the existence of a source of hydrogen not directly dependent on the gas content of the samples tested. This has been clear from the

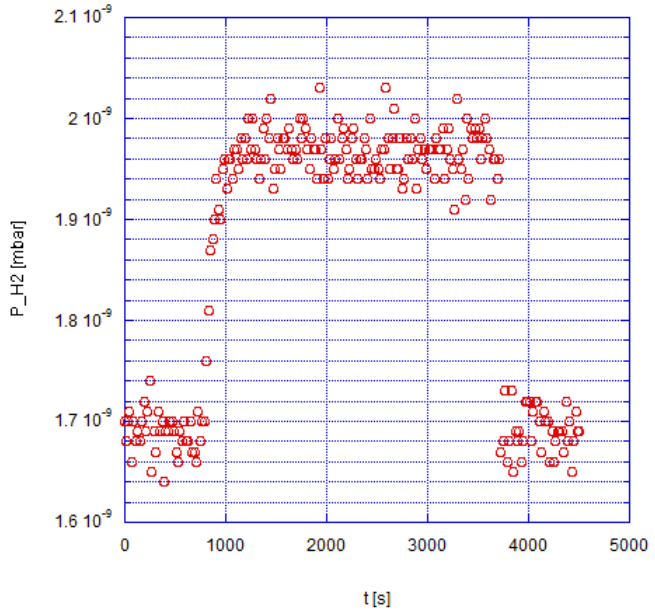

Figure 4.9: Hydrogen pressure during outgassing experiment

very beginning of this study, when a silicon sample, in which no hydrogen content is expected, was tested with the previous described setup and a huge increase in hydrogen partial pressure was noticed.
The following efforts were done in the direction of investigate, evaluate (more details can be found in 4.2.3)and eventually mitigate this source, most probably related to electrons and ions stimulated desorption from the wall of the vacuum chamber.

Buffer gas

The desorption induced by electrons and ions is a well-known phenomenon (the first part of this work have dealt with ESD). During ablation In the system To avoid or at least reduce the weight on hydrogen present in chamber, the injection of a "buffer gas" has been proposed. The gas that have been considered are a noble gas and a molecular gas, both with a low vapour pressure at liquid nitrogen temperature to exploit the trapping capability of the cold trap as much as possible: Xe ($P_{vap@77K} \sim 10^{-4} mbar$) and CO_2 ($P_{vap@77K} \sim 10^{-8} mbar$). The idea is to slow down the charged particles produced in the plasma during ablation by means

of elastic collision with the buffer gas. The electrons, anyway, can easily ionize the gas leading to have more charged particle around and so worse experimental conditions. The CO_2 has a lower electrons impact induced ionization probability than Xe, is more electronegative and has more ways to absorb energy in inelastic way especially for low energy electrons: excitation of vibrational states. However CO_2 is more chemical reactive than Xe and could induce some unwanted effects on the surfaces of materials.
In the beginning ablation experiments have been done injecting dynamically the buffer gas in the AB chamber. The data are shown in Figure 4.10: the released hydrogen decreases slightly as the pressure of the injected Xenon rises. This behaviour seems to validate the effectiveness of the role of buffer gas, deeply investigate at a later stage of the development of the measurement process.

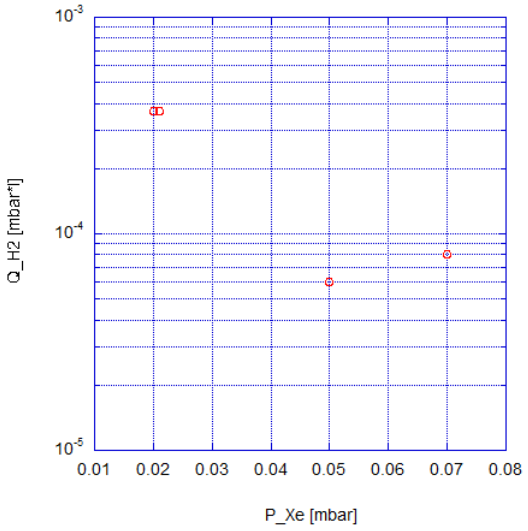

Figure 4.10: Hydrogen release in ablation of silicon at different buffer gas (Xe) pressure.

Detection of electrons

In section 2.2 an overview of different ablation induced ionization phenomena has been given. Electrons and ions are always produced and the detection of them can be used as a probe to investigate to which regime of laser-target interaction the

sample is subject.
The measure and collect electrons a filament, located inside the chamber at about 6 *cm* distance of target, is used. A fast oscilloscope measures the variation of a negative voltage V on this filament, once is positively biased.(See Figure 4.11 for circuital scheme). The measurement has been taken usually for $V_1 = 18\ Volt$ (i.e. two 9 $Volts$ batteries in series) but it has been checked that it do not change a lot for higher (up to 100 V) voltage.

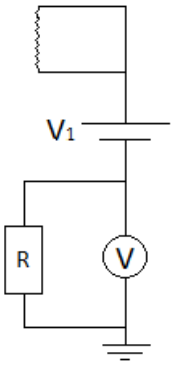

Figure 4.11: Electrical circuit for detection of electrons

The typical track on the oscilloscope has the pulsed shape shown in Figure 4.12.
The purpose of this experimental setup is to have a probe with which investigate the ablation phenomenon. In particular it was interesting to inquire the existence of a threshold depending on the fluence and the material, but also the influence of buffer gas has been tested with this setup.
The most important data acquired are shown in Figure 4.13, Figure 4.14 and Figure 4.15.
For each point the sample has been shot by the laser, while recording the current on filament, 5 different times. Afterwards, integrating the current pulse over time, the number of collected electrons has been calculated.
As indicated by errors bars the number of collected electrons vary strongly from one laser shot to an other. This feature it is not surprising as the phenomenon is very complex and most probably the filament can trap only a part of the whole number of the involved electrons of the electrons involved.
The average values shows a clear trend: the number of collected electrons increases

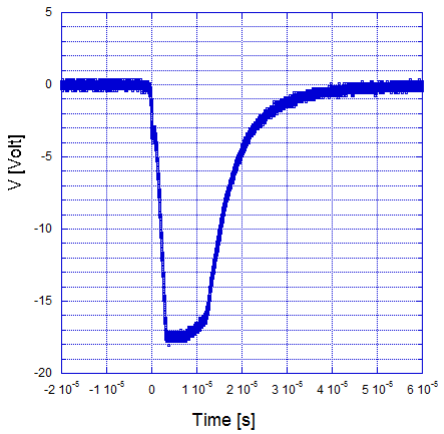

Figure 4.12: Track on the oscilloscope for 18 Volt biasing, ablation on copper sample, 5 J/cm^2 fluence

as the fluence is raised but sharply after a certain fluence value.
For the copper this threshold value is collocated in $2 \div 3$ J/cm^2 while for titanium can be put at $\sim$ 2 J/cm^2. In Figure 4.14 the onset of the proportional trend is less evident due to the scale of the graphs, but to deeper investigation can be found in the range of $3 \div 4$ J/cm^2. The general behaviour, was confirmed for UHV condition and different buffer gases as well as different materials. Therefore the number of collected electrons can be interpreted as an indicator of the effectiveness of the ablation. Moreover it is possible to infer several features from this measurements.

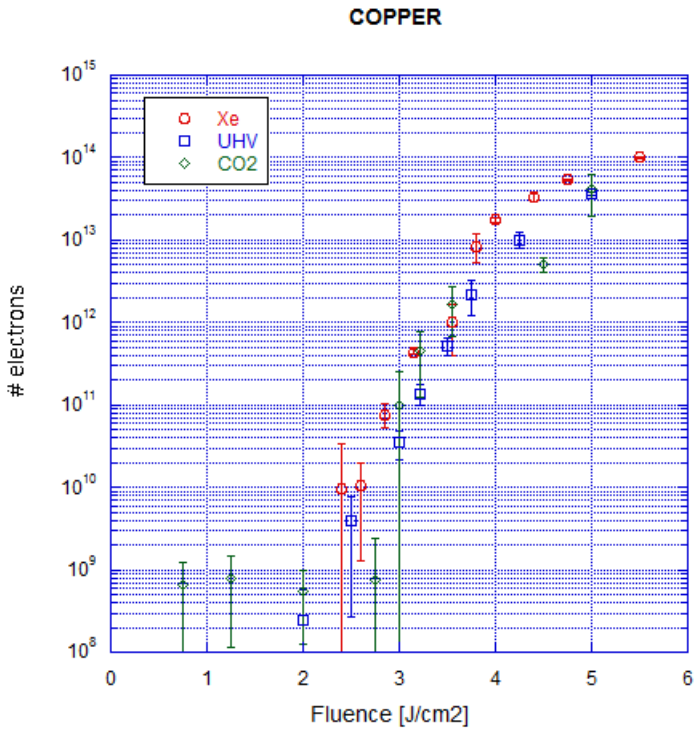

Figure 4.13: Electrons collected on the filament over fluence for shot on Copper

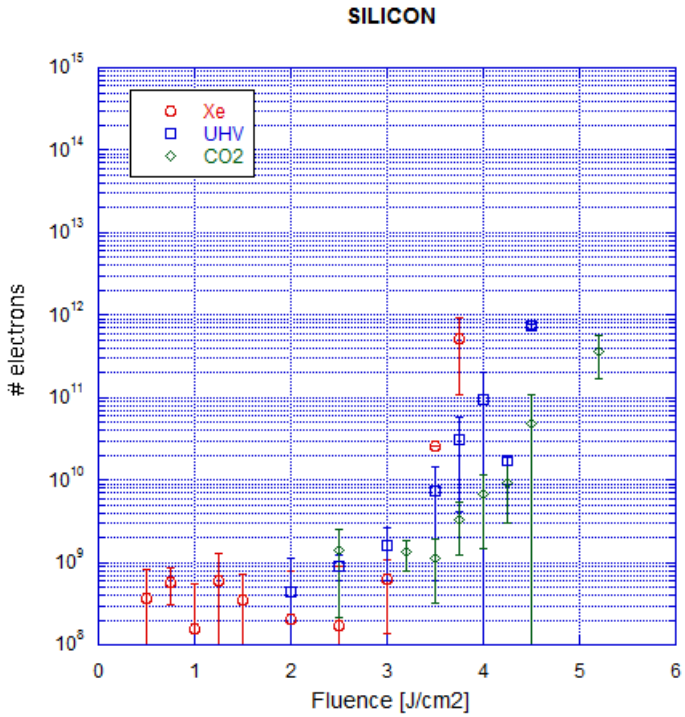

Figure 4.14: Electrons collected on the filament over fluence for shot on Silicon

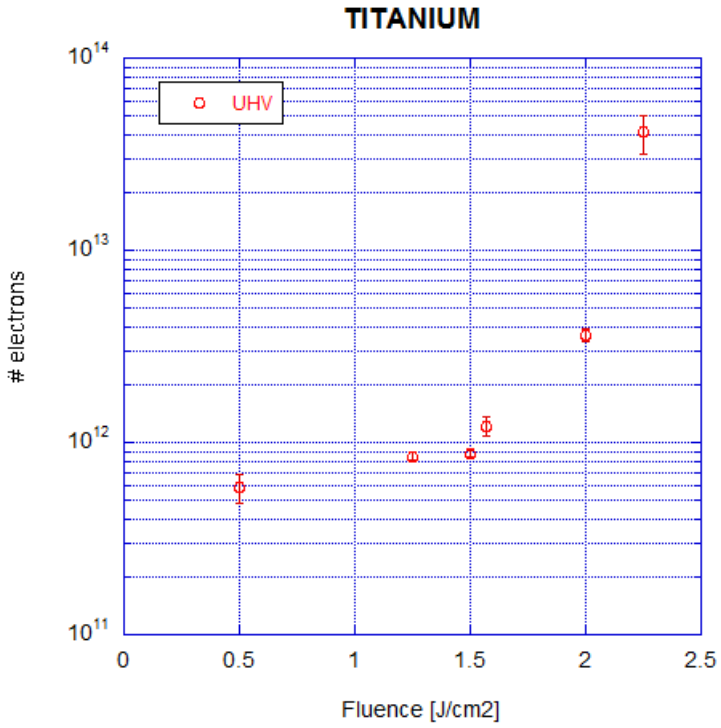

Figure 4.15: Electrons collected on the filament over fluence for shot on Titanium

Comparison of the measured threshold with the values found in the literature will be done hereafter.

1. The plasma threshold can be defined as the laser fluence at which two different conditions are fulfilled concurrently: the metal surface is heated to the boiling point to provide metal vapour and ,secondly, the laser intensity is high enough to enable dielectric breakdown in the vapour.[24] Both the thermodynamic response and the plasma generation are associated with a pressure wave crated in the surrounding medium. However the target heating results in an ordinary sound wave whereas the expansion of a laser induced plasma produces a shock wave. An acoustic mirage effect technique, by means of which it is possible to distinguish between the two different waves, has been used to investigate the phenomenon.
   They found a plasma threshold fluence for nanosecond laser pulses on copper of 3 J/cm^2 and on titanium of 2 J/cm^2.

2. It is possible to define the onset of optical breakdown in a vapour plume generated at a UV-laser-heated surface in a different way. Theoretical prediction obtained by means of a simplified model and experimental measurements have been done for Copper, Silicon and Titanium [25]. The model takes into account only the photoionization process and defines the onset of the breakdown as the point at which the rate of temperature rise of the ablation plume exceeds that of the target surface, while in the experiments "significant" ion emission has been measured by monitoring optical-UV emission line with a monochromator. The results are shown in Table 4.3.

	Data x10^8 W/cm^2	Model x10^8 W/cm^2
Copper	0.60	1.44
Silicon	1.19	2.10
Titanium	0.65	0.25

Table 4.3: Experimental and modeled breakdown irradiances for an excimer laser (KrF, $\lambda = 248nm$) and pulse 21 ns long

In the first case there is a clear agreement for the absolute value of the plasma thresholds. For the second case, instead, one can say that the relative position of fluence threshold is respected founding the lowest value for ablation of titanium and the highest for silicon.
Moreover the data shown in Figure 4.13 and Figure 4.14 have lead to assume that the influence of buffer gas is negligible. In fact, as the fluence is the same, in the case of buffer gas injected there is a small difference in the absolute number of collected electrons compared to the case of UHV environment. Probably the effect for electrons would be stronger at very high pressure(see Figure 4.16). To avoid all the problems involved with the injection of a gas, first of all the influence on the RGA sensitivity, the following ablation experiments have been performed in UHV condition.

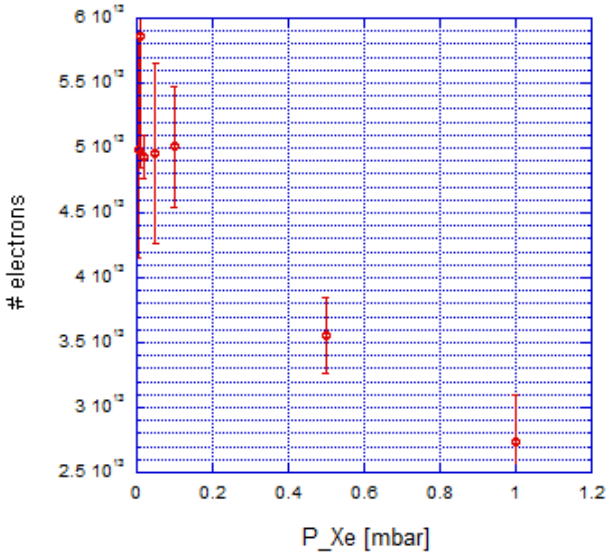

Figure 4.16: Number of electrons collected on the filament over Xenon pressure for ablation on Copper sample

The number of collected electrons related to the ablation of copper are always almost two order of magnitude higher than the case of ablation on silicon. Once the threshold is achieved, probably, the ionization in the vapour at the copper surface is stronger leading to more electrons.

There's anyway a need to gain better understanding of the actual meaning of the collected electrons and the relation with all the charged particles involving the ablation phenomenon.

The same procedure, except for the negative bias on the filament, was attempted to collect ions. The signal recorded by the oscilloscope showed a huge instability from one shot to an other. The difficulty in trapping ions could be the explanation. However the measurement has been given up.

Trap for charged particles

The idea to trap charged particles biasing the sample holder with high voltage has been taking into consideration.
Ablation experiments have been performed with sample holder biased at 500 $Volts$, both positively and negatively. The hydrogen release in the previous configurations has been compared to the measurement taken with grounded sample holder. The release, for both the positive and negative bias, is almost one order of magnitude more than the measurement with grounded sample holder.
Except for the fluence, the specific of the experiment are always the same: 20 shot on stainless steel sample at a frequency of 20 Hz repeated 3 times. As in case of grounded sample the pulse energy was lower, the difference in released quantity is ascribable to that.
The trial has been considered unsuccessful but leads to infer something more. In both case, positive or negative bias, the released hydrogen is almost the same even if the ions induced desorption should be higher than electrons stimulated desorption. [28] It is know that same-charge particles have a different behaviour depending on their mass. The electrons are quickly accelerate towards the positive voltage while the ions have a slower dynamic. The ions have a bigger inertia and it is more difficult to deviate their trajectories, which are drive by the plasma diffusion. The electric trap, therefore, can be effective for the majority of electrons but not for the ions. The ions go towards the wall of the chamber and the induced desorption from the wall is mostly due to them.

Photodesorption and photoemission leading to ESD

One explanation of the huge amount of molecules recorded during ablation experiments could be laser interaction with sample holder. The photons could induced desorption from the sample holder (*photodesorption*) or produce electrons (*photoemission*) which in turn cause ESD from the surfaces of the system.
To investigate the validity of this hypothesis the released quantity of hydrogen has been detected while the sample holder has been shot by unfocussed laser beam.
No peaks were found in the the hydrogen partial pressure recorded over time, leading to reject the direct photons induced effects as source of "dynamic hydrogen background".

4.2.3 Data

Several experimental attempts, following the steps described in section 4.2, has been done to investigate the limits of the setup and improve, where possible, the measurement process. The data related to some of these experiments will be presented in this section as they have been acquired.
Firstly ablation on a silicon sample has been performed to estimate the hydrogen background (already treated in section 4.2.2), not related to the content in the samples.

Silicon

The tested silicon samples have not been treated in hydrogen atmosphere and, moreover, the hydrogen solubility in silicon is low. For instance, after 1 hour in a hydrogen plasma at 200^oC the concentration reached is of $\sim 10^{18}$ (i.e. $\sim 10^{18} H\ at/Si\ at$) in a layer $\sim 1\ \mu m$ thick [27].
Therefore the silicon sample was useful to have a measure of the hydrogen background. During ablation different masses are recorded by RGA, for ablation on silicon the trend over time is shown in Figure 4.17.
The value recovered after the peak, that is a little higher after every ablation event, is substracted from highest pressure value before the integration over time.
The values for the hydrogen released Q_{H_2}, calculated from the measured data, are shown in Table 4.4. In particular for $2\ 10^{-2}\ mbar$ and $7\ 10^{-2}\ mbar$ were confirmed twice.

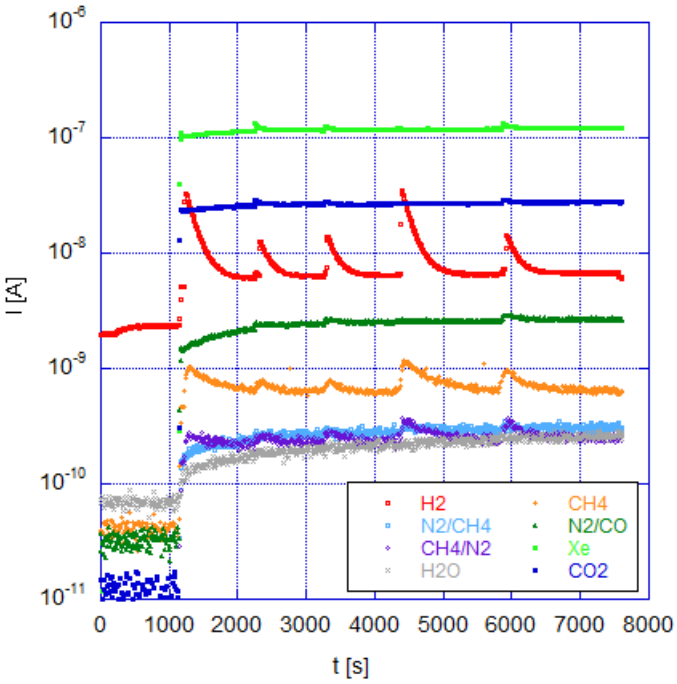

Figure 4.17: RGA signal for different masses as a function of time measured during ablation on silicon sample(xenon injected)

$P_{Xe}[mbar]$	$Q_{H_2}[mbar \times l]$
$2\ 10^{-2}$	$3.7\ 10^{-4}$
$5\ 10^{-2}$	$6\ 10^{-5}$
$7\ 10^{-2}$	$8\ 10^{-5}$

Table 4.4: Hydrogen release measured during ablation on silicon

The resulting values are very high and cannot be ascribed to the ablation on silicon. These results therefore suggest the presence of a "parasitic" source of hydrogen.

Copper

In section 2.3 the expected content in copper sample was estimated. It is possible to calculate the associated hydrogen release, assuming a certain value for ablated volume (it was not possible to measure the actual value).
The volume ablated v_{abl} can be estimate considering the area of the spot (2 mm^2) and 1 μm for the thickness of evaporated material (this value is probably an overestimate).
The number of degassed hydrogen molecules n_{H_2} is:

$$n_{H_2} = 2\frac{\chi_H \ \rho_{Cu} \ v_{abl} \ N_{Av}}{M_{Cu}} \tag{4.8}$$

where $\chi_H = 70$ ppm is the expected content of hydrogen in the sample, $\rho_{Cu} = 8.92$ g/cm^3 and $M_{Cu} = 63.5$ g are the copper density and the copper atomic weight, $N_{Av} = 6.022 \cdot 10^{23}$ is the Avogadro constant. Using the ideal gas law, the pressure increase Δp_{H_2} ascribed to this amount of molecules is:

$$\Delta p_{H_2}[mbar \times l] = 10^{-2} n_{H_2} \cdot k \cdot T \tag{4.9}$$

where $k = 1.38110^{-23}$ J/K is the Boltzmann constant and $T = 300$ K is the ambient temperature. Solving equation (4.8) one gets $\Delta p_{H_2} = 2.6410^{-7}$ $mbar \times l$, which is over two order of magnitude below the background.
Experimental evaluation on copper samples confirmed the huge value of background estimated by means of ablation on silicon. In Table 4.5 the data for ablation on copper (10 shots at 5 Hz, 6 J/cm^2 fluence) are given.
Ablation experiments on the same copper sample were done in UHV condition with a beam of fluence of 5 J/cm^2. The RGA signal related to hydrogen is shown in Figure 4.18 while the results obtained after data analysis are listed in Table 4.6(given in the sequence of the measurement).
It appears as expected that the more laser pulses hit the sample the higher are the pressure peaks, while the frequency does not influence significantly the amount of gas release. Shot more times it is possible to remove more materials indeed.
However the values obtained for 10 shots are in the same range for both UHV

$P_{Xe}[mbar]$	$Q_{H_2}[mbar \times l]$
$4.5\ 10^{-2}$	$4.37\ 10^{-4}$
$6.5\ 10^{-2}$	$4.37\ 10^{-4}$
$7\ 10^{-2}$	$2.4\ 10^{-4}$
$19\ 10^{-2}$	$9.69\ 10^{-5}$

Table 4.5: Hydrogen release measured during ablation on copper for xenon injection at different pressure

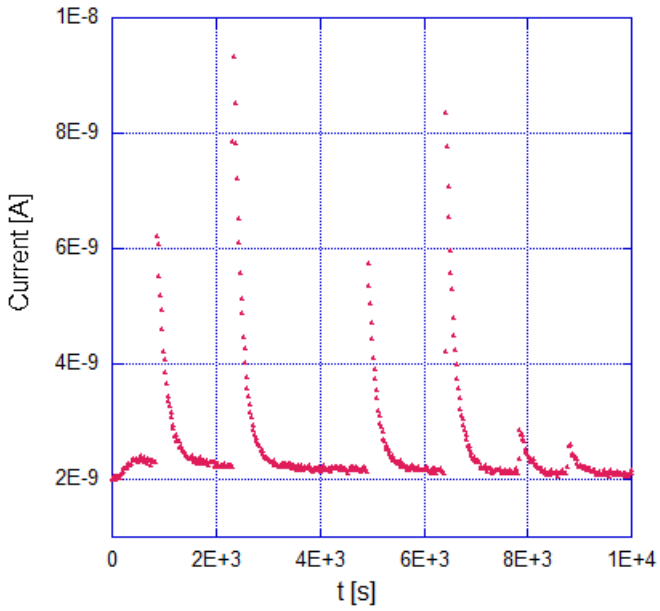

Figure 4.18: RGA signal for hydrogen as a function of time measured during ablation on copper sample (UHV condition)

Parameters	$Q_{H_2}[mbar \times l]$
100 shots, 100 Hz	5.70 10^{-3}
100 shots, 5 Hz	9.56 10^{-3}
100 shots, 100 Hz	5.06 10^{-3}
100 shots, 5 Hz	8.71 10^{-3}
10 shots, 100 Hz	1.16 10^{-3}
10 shots, 5 Hz	6.89 10^{-4}

Table 4.6: Hydrogen release detected during ablation on copper in UHV

condition and xenon injected. This confirm that the effect of "buffer gas" is negligible.

Titanium

A further investigation of this hydrogen-content-measurement method was done cross-checking the results from ablation on untreated titanium and titanium after thermal treatment. The latter has been treated in a furnace with a hydrogen pressure of 25 $mbar$. In section 2.3 the expected content in treated titanium sample was estimated. It is possible to do the same calculation done for copper in order to obtain the hydrogen release related to ablation on titanium.
Solving (4.8) and (4.9) for $\rho_{Ti} = 4.51\ g/cm^3$ and $M_{Ti} = 47.87$ and $\chi_H = 4.75\ 10^4 ppm$ the expected hydrogen release is:

$$\Delta p_{H_2} = 1.4 \cdot 10^{-4}\ mbar \times l \tag{4.10}$$

This value can be compared to the background pressure due to outgassing, which is in the range of $10^{-5}/10^{-4} mbar * l$. Therefore the expected quantity is bigger than the outgassing contribute and moreover, in this case, it is possible to compare the result with a standard sample of titanium not treated.
The released hydrogen quantity are listed in Table 4.7 for ablation on treated titanium sample.
In Table 4.8 are shown data for not treated Titanium sample (given in the sequence of the measurement).

Parameters	$Q_{H_2}[mbar \times l]$
100 shots, 5 Hz	$9.27\ 10^{-5}$
100 shots, 5 Hz	$1.13\ 10^{-4}$
100 shots, 5 Hz	$1.24\ 10^{-4}$
1000 shots, 5 Hz	$3.3\ 10^{-3}$

Table 4.7: Hydrogen release detected during ablation on treated titanium samples in UHV

Parameters	$Q_{H_2}[mbar \times l]$
100 shots, 5 Hz	$4.43\ 10^{-4}$
100 shots, 5 Hz	$5.19\ 10^{-4}$
100 shots, 5 Hz	$5.97\ 10^{-4}$
1000 shots, 5 Hz	$1.89\ 10^{-3}$

Table 4.8: Hydrogen release detected during ablation on not treated titanium samples in UHV

The calculated amount seems to be not related, once again, to the actual content of hydrogen. Moreover the results obtained for not treated titanium sample are almost always bigger than the results for the other titanium sample which is supposed to have a huge amount of hydrogen after the heat treatment.

4.3 Discussion and Outlook

The sensitivity in the measurement of the hydrogen release during ablation is related first of all to the huge hydrogen background of the system. The hydrogen background has to be meant as normal degassing of chamber plus the dynamic background related to ablation but not due to the content in the samples.

The first source cannot be removed. It has to be noted that every single time the system has been opened, 24 hours bake-out of the vacuum chambers and degassing of the Bayard-Alpert gauge and the RGA filaments has followed the pump down. Moreover, the pressure in the AN chamber was always in the range of $10^{-10} \div 10^{-9}\ mbar$.

The second source has been investigated. It was concluded that the ions induced desorption from the wall seems to be the real source of the hydrogen background. Several attempts has been done to remove Tor at least mitigate this source. The buffer gas does not avoid ions to imping on the wall of the chambers. Moreover it was not possible to trap the ions even biasing sample holder with voltage up to $500\ V$. However none of the above mentioned methods seems to be successful.

An other parameter affecting the measurement is the sensitivity of the RGA, which needs to be recalibrated frequently but nevertless showed to have an uncertainty of about 30%.

As expected, the number of shot influence the released quantity. The frequency of pulses, however, do not have any influence. Assuming that the plasma time scale is of the order of microseconds, a different frequency of pulses in the range of $5 \div 100\ Hz$ has no effects.
It was not possible to have an evaluation of the volume ablated for most of the sam-

ples. The measurement acquired from the metrology department, using a white light interferometer, were not reliable. Probably this was due to the roughness of the samples.

Moreover, this work dealt with some troubleshooting related to the quarz window in between the lens and the samples: after a while the detection of electrons for ablation on copper gave significantly different values in comparison to the first measurement. As usual to evaluate the fluence the pulse energy has been measured after the last lens with the Joulemeter.
After removing the viewport, the transmittance of the window was tested: almost 30% of attenuation has been found. Possible explanations are metalization of the window (due to sputtering of metal) or defect generation and propagation in the chrystallographic structure due to the high irradiance.It has to be pointed out that the distance between the lens and the samples is almost 10 cm, so the fluence is high at the quarz surface (refer to section 4.1.2 for optical system layout). To determine if and when this phenomen has started, the "recipe" for the next measurements has been to detect electrons during the ablation experiments in order to be sure that the fluence values is the desired one (for correlation between fluence and number of detected electrons see section 4.2.2).
However the quick damage of the window can be listed in the limitations of such a setup.
Considering all the mentioned limitations of the system, one would state that the method described in this chapter is not suitable for hydrogen content measurement in metals due to the parasitic hydrogen outgassing.

Chapter 5

Summary

The CLIC accelerating structures, due to their manufacturing and their operational conditions (high accelerating gradient), have raised several problems concerning the vacuum requirements.
Static and dynamic vacuum effects of OFE copper need to be investigated in order to find the best cleaning and heat treatment, to fulfil these requirements.

In the first part of this work, one sample of the campaign has been tested with the existing ESD measurement system. The desorption yield shows the expected decreasing trend with increasing electron dose, meaning that the surface is "conditioning" by the impinging electrons. Furthermore, the dependence of the desorption yield on the electron energy has been investigated, confirming the theoretical prediction.
The desorption yield values for the copper sample, thermal treated under 1 bar of hydrogen (54-SSH104C), are almost one order of magnitude lower than the data related to the previously tested sample (19-V082C, which was treated under vacuum). One would expect a higher hydrogen desorption from the former sample. Therefore, the behaviour of the material is probably mostly influenced by the storage condition as well as the time the sample has stayed in air. These experimental data will be useful, after cross-checking with the other tests of the copper samples of the campaign, to choose the best solution for the CLIC accelerating structures.

The second part of this work aimed to investigate the possibility of hydrogen con-

tent measurement in copper by a laser ablation setup. Hydrogen can easily diffuse into the bulk of metals and even more during the bonding cycles of the CLIC accelerating structures, which are performed at high temperature and under hydrogen atmosphere. An experimental setup to determine the atomic concentration of hydrogen would be very useful to predict the behaviour of copper.
A laser ablation experiment on metals coupled with the measurement of the resulting hydrogen partial pressure increase, has never been investigated before, to our knowledge. This method could be competitive with other measurement techniques, from a theoretical point of view. However several experimental limits have been encountered.
The source of hydrogen background pressure, i.e. hydrogen release not related to the actual hydrogen content in the sample, was investigated.
The interaction of the laser with the target at high irradiance produces a plasma. The resulting ions can be accelerated towards the wall of the chamber during the plasma dilation. Therefore the most probable explanation for the source of dynamic hydrogen background is the desorption from the wall of the vacuum chamber induced by ions generated in that plasma.
Several attempts have been made but it was not possible to reduce it.
Therefore the hydrogen content in metals measurement does not seem to be feasible with the experimental setup described in the previous chapter.

Bibliography

[1] *The Compact Linear Collider Study official web-site* http://clic-study.org

[2] H. Timko, *Arcing and plasma-wall interactions*, M.sc Thesis, 2008

[3] A. Descoeudres et al.: *Dc breakdown conditioning and breakdown rate of metals and metallic alloys under ultrahigh vacuum*, Phys. Rev. ST Accel. Beams 12, 032001 (2009)

[4] A. Descoeudres et al.: *Investigation of the dc vacuum breakdown mechanism*, Phys. Rev. ST Accel. Beams 12, 032001 (2009)

[5] M. Kildemo: *New spark-test device for material characterization*, Nucl. Instrum. Meth. A 530, 596-606 (2004)

[6] http://www.chembio.uoguelph.ca/educmat/chm729/esdiad/main.htm

[7] D.Menzel, *Thirty years of MGR: How it came about and what came of it*, Nuclear Instruments and Methods in Physics Research B 101, (1995)

[8] ,D.Menzel,R.GOmer *Desorption from Metal Surfaces by Low-Energy Electrons*, Journal of Chemical Physics, Vol. 41, Nb. 11, (Dec. 1964)

[9] P.R. Antoniewicz *Model for electron and photon stimulated desorption*, Physical Review B, Vol. 21, Nb. 9, May 1980

[10] Z.W.Gortel, *Beyond MGR: Wave packet squeezing*, Nuclear Instruments and Methods in Physics Research B 101, (1995) 11-21

[11] E. Fromm, W.Hehn, G.Horz, *Gases and Carbon in Metals: Thermodynamics, Kinetics and Properties. Copper*,Max-Planck-Institut fr Metallforschung, Stuttgart, Germany, 1984

[12] H.Jehn, H.Speck, E.Fromm, G.Horz, *Gases and Carbon in Metals: Thermodynamics, Kinetics and Properties. Titanium*,Max-Planck-Institut fr Metallforschung, Stuttgart, Germany, 1984

[13] B. Henrist, N.Hilleret, C.Scheuerlein, M.Taborelli, G.Vorlaufer, *The variation of the secondary electron yield and of the desorption yield of copper under electron bombardment: origin and impact on the conditioning of LHC*, CERN, Geneva, Switzerland

[14] P.Avouris, R.E.Walkup, *Fundamental mechanism of desorption and fragmentation induced by electronic transitions at surfaces*, Annu. Rev. Phys. Chem. 189.40:173-206

[15] F.Billard, N.Hillert, G.Vorlaufer, *Some results on the electron induced desorption yield of OFHC copper*, Vacuum technical Note 00-32, Dec 2000

[16] C.Pasquino, *Electron stimulated desorption of OFE copper for particle accelerators*, M.sc. Thesis, (2011)

[17] J.M.Lafferty, *Foundations of vacuum science and technology*, Wiley-Interscience, (1998)

[18] K.H. Bernhardt, *Vacuum technology compendium*, Pfeiffer Vacuum GmbH, (2010)

[19] G. F. Knoll,*Radiation Detection and Measurement*, John Wiley and Sons Inc.

[20] NIST, ESTAR database, *Stopping power and range tables for electrons*, www.nist.gov

[21] M. von Allmen, A.Blatter, *Laser-Beam Interactions with Materials: Physical Principles and Applications*, Springer Series in Material Science 2 (Springer, Berlin, 1987)

[22] E.G. Gamaly, A.V.Rode, B. Luther-Davies, *Laser ablation of carbon at the threshold of plasma formation*, App. Phys. A 69[Suppl.], S121-S127 (1999)

[23] C.Benvenuti, S.Calatroni, J.Carver, P.Chiggiato, S.Clair, H.Neupert, W.Vollenberg, *Study of discherge gas trapping during thin film growth*, Vacuum 60 (2001) 89-94

[24] S. Petzoldt,J. Reif, E. Matthias, *Laser plasma threshold of metals*, Applied Surface Science 96-98 (1996) 199-204

[25] P.Clarke, P.E. Dyer, P.H. Key, H.V. Snelling, *Plasma ignition thresholds in UV laser ablation plumes*, Appl. Phys.A 69 [Suppl.], S117-S120 (1999)

[26] B.Salle, C Chaleard, V.Detall, J.L.LAcour, P.Mauchien, C.Nouvellon, A.Semerok, *Laser ablation efficiency of metal samples with UV laser nanosecond pulses*, Applied Surface Science 138-138 (1999) 302-305

[27] , M. Stavola, *Hydrogen in Silicon and Germanium*, The 5th International Symposium on Advanced Science and Technology of Silicon Materials (JSPS Si Symposium)

[28] G. Hulla, *Low energy ion induced desorption on technical surfaces at room temperature.* M.sc. Thesis, (2009)